2004

High-resolution Imaging of Dust Shells Using Keck aperture Masking and the IOTA Interferometer

J. D. Monnier
University of Michigan - Ann Arbor

R. Millan-Gabet
California Institute of Technology

P. G. Tuthill
University of Sydney

W. A. Traub
Harvard-Smithsonian Center for Astrophysics

V. Coudé du Foresto
Observatoire de Paris-Meudon

See next page for additional authors

Recommended Citation
Monnier, J. D.; Millan-Gabet, R.; Tuthill, P. G.; Traub, W. A.; Coudé du Foresto, V.; Danchi, W. C.; Lacasse, M. G.; Morel, S.; Perrin, G.; Porro, I. L.; Schloerb, F. P.; and Townes, C. H., "High-resolution Imaging of Dust Shells Using Keck aperture Masking and the IOTA Interferometer" (2004). *Astronomy Department Faculty Publication Series*. 14.
10.1086/382218

High-resolution imaging of dust shells using Keck aperture masking and the IOTA Interferometer

J. D. Monnier[1], R. Millan-Gabet[2], P. G. Tuthill[3], W. A. Traub[4], N. P. Carleton[4], V. Coudé du Foresto[5], W. C. Danchi[6], M. G. Lacasse[4], S. Morel[7], G. Perrin[5], I. L. Porro[8], F. P. Schloerb[9], and C. H. Townes[10]

ABSTRACT

We present first results of an experiment to combine data from Keck aperture masking and the Infrared-Optical Telescope Array (IOTA) to image the circumstellar environments of evolved stars with ∼20 milliarcsecond resolution. The unique combination of excellent Fourier coverage at short baselines and high-quality long-baseline fringe data allows us to determine the location and clumpiness of the inner-most hot dust in the envelopes, and to measure the diameters of the underlying stars themselves. We find evidence for large-scale inhomogeneities in some dust shells and also significant deviations from uniform brightness for the photospheres of the most evolved M-stars. Deviations from spherically-symmetric mass loss in the red supergiant NML Cyg could be related to recent evidence for dynamically-important magnetic fields and/or stellar rotation. We point out that dust shell asymmetries, like those observed here, can qualitatively explain the difficulty recent workers have had in simultaneously fitting the broad-band spectral energy distributions and high-resolution spatial information, without

[1]monnier@umich.edu: University of Michigan Astronomy Department, 941 Dennison Bldg, Ann Arbor, MI 48109-1090, USA.

[2]Michelson Science Center, California Institute of Technology

[3]University of Sydney, Physics Department

[4]Harvard-Smithsonian Center for Astrophysics, 60 Garden St, Cambridge, MA, 02138, USA

[5]Observatoire de Paris-Meudon

[6]NASA Goddard Space Flight Center

[7]European Southern Observatory

[8]Massachusetts Institute of Technology

[9]University of Massachusetts, Amherst

[10]University of California, Berkeley

invoking unusual dust properties or multiple distinct shells (from hypothetical "superwinds"). This paper is the first to combine optical interferometry data from multiple facilities for imaging, and we discuss the challenges and potential for the future of this method, given current calibration and software limitations.

Subject headings: instrumentation: interferometers — techniques: interferometric — stars: AGB and post-AGB — stars: atmospheres — circumstellar matter

1. Introduction

Since the advent of infrared detectors, the classic tool for studying circumstellar dust shells has been fitting the spectral energy distributions (SEDs) using radiative transfer models. This has been true for stars across the Hertzsprung-Russell diagram, for young stars still accreting material as well as for evolved stars with their winds. The conclusions of these studies are only beginning to be tested rigorously through high-resolution imaging in the visible and infrared, using 8-m class telescopes and long-baseline interferometers.

In this paper, we focus mainly on dust shells around evolved stars. Almost all evolved star SEDs can be fitted well using a simple physically-realistic model including a star and a spherically-symmetric, uniform-outflow dust shell (e.g., Rowan-Robinson & Harris 1982; Ivezic & Elitzur 1996b). This success led to initial confidence in our understanding of mass-loss mechanisms: that dust condenses at T$\sim$1000-1500 K out of a dense stellar atmosphere with a scale height larger than hydrostatic, maintained by shocks launched from photospheric pulsations (see recent reviews by Hearn 1990; Lafon & Berruyer 1991; Habing 1996). This theory makes definite predictions for what should be observed when high-resolution imaging can resolve these objects, both in terms of location and nature of the dust formation and the time evolution as clouds are accelerated away from the star by radiation pressure.

Although early speckle results of Dyck et al. (1984) found near-IR dust shell sizes consistent with expectations (given the limited spatial resolution), recent higher-resolution imaging and interferometry have consistently found strong deviations from a simple mass loss scenario. The Infrared Spatial Interferometer (ISI) found evidence for diverse dust shell properties in their survey of 13 stars (Danchi et al. 1994). More dramatically, recent speckle and aperture masking images of the carbon star IRC+10216 have revealed inhomogeneities and asymmetries on stellar scales (Haniff & Buscher 1998; Weigelt et al. 1998; Tuthill et al. 2000a); only a few years earlier, a spherically-symmetric, uniform-outflow model was successfully fit to the SED (Ivezic & Elitzur 1996a). Virtually every recent published attempt to incorporate high-resolution spatial information into SED models has led to the conclusion

that there are strong deviations from the simple mass-loss prescription of uniform outflow and spherical symmetry. (e.g., Monnier et al. 1997; Lopez et al. 1997; Hale et al. 1997; Monnier et al. 1999b; Wittkowski et al. 1998; Gauger et al. 1999; Blöcker et al. 1999; Hofmann et al. 2001), at least for the most evolved and dust-enshrouded sources.

While SED models are adequate for estimating some basic parameters about dust shells and mass-loss rates (average optical depth and temperatures), they can not definitively answer some important questions regarding dust condensation conditions, grain properties, and the basic mass-loss mechanisms (e.g., source of wind energy and atmospheric extension). High-resolution observations, however, can potentially answer these questions by imaging dust as it forms and accelerates away from the star. This morphology and dynamical information is much better for constraining the wind and mass-loss theories. Current interferometer technology is beginning to provide this: "movies" of the expanding dust shell around IRC +10216 are already available (Tuthill et al. 2000a; Weigelt et al. 2002).

Until recently, high-resolution images of dust shells could only be made of the "biggest" sources using aperture masking and speckle interferometry. In this paper, we extend the capability to ∼20 milliarcsecond scales by combining Keck aperture masking data, which samples baselines up to 9 m, with IOTA interferometer data, which samples out to 38 m. By constraining the long-baseline visibility, we are able to make higher fidelity images of the inner dust shells. This allows us to measure the inner radius of dust condensation and to search for signs of dust shell asymmetry and clumpiness, information critical to validating (or falsifying) our current theories of mass loss.

Lastly, we want to connect our efforts to image evolved stars with beginning efforts to image disks around Young Stellar Objects (YSO). The history of YSO SED modeling is beginning to resemble the history for evolved stars recounted above. Interferometry results (Millan-Gabet et al. 1999; Akeson et al. 2000; Millan-Gabet et al. 2001; Tuthill et al. 2001; Akeson et al. 2002; Monnier & Millan-Gabet 2002; Tuthill et al. 2002; Colavita et al. 2003) have found profound differences from the predictions of the "successful" disk models based on fitting to SEDs alone (Hillenbrand et al. 1992; Hartmann et al. 1993; Chiang & Goldreich 1997). The new high-resolution imaging techniques developed here will soon be applied to imaging preplanetary disks around young stars using new interferometer facilities, such as the Center for High Angular Resolution Array (CHARA).

The organization of this article is as follows. We begin by describing the nature of the observations and the facilities used to acquire the high resolution data. Next, we describe the data analysis, including the results of extensive validation experiments using new observations of RT Vir, R Leo, R Hya, and W Hya (an appendix details our novel calibration method). We then discuss the results on each of the "dust shell" targets: HD 62623,

IRC +10420, VY CMa, NML Cyg, VX Sgr, and IK Tau. These analyses include diameter fitting, radiative transfer modeling, and image reconstructions. We also include a general discussion regarding the difficulties in imaging with new optical interferometers.

Future papers will take up the challenge of creating self-consistent 2-D or 3-D radiative transfer models of the individual sources. Considering the increased interest in this area recently, this paper provides an important and timely dataset for other modellers of evolved stars and dust shells.

2. Observations

In this study, we combine data obtained using aperture masking on the Keck-I telescope (Tuthill et al. 2000b; Monnier 1999) and using the FLUOR (Fiber Linked Unit for Optical Recombination) beam combiner (Coude Du Foresto et al. 1998) on the IOTA (Infrared-Optical Telescope Array) interferometer (Traub 1998). The circumstellar environments of evolved stars are known to change with time, both due to variable mass-loss on the many-year timescale (e.g., Haniff & Buscher 1998; Monnier et al. 1997) and due to large-amplitude pulsations on shorter timescales (Danchi et al. 1994; Perrin et al. 1999). Thus, coordinated (near simultaneous) observations at both facilities were deemed critical to avoid possible changes in dust shell morphology between observations.

Here we report on all dust shell targets of this aperture synthesis effort except for the carbon star V Hya, the subject of a separate paper (Millan-Gabet, in preparation), and Table 1 lists the target sources and their basic properties. Table 2 contains a full journal of our observations relevant to this paper, where it can be seen that Keck and IOTA measurements were typically made within a month of each other. In some cases (detailed later), we have also included data from other epochs for comparison. While all observations were done inside the astronomical K-band (2.0-2.4μm), the Keck data used narrow band filters while the IOTA/FLUOR experiment used a broad band K$'$ filter; this and other factors lead to systematic errors which are discussed fully in section §3.3.

2.1. Aperture Masking

Aperture masking interferometry was performed by placing aluminum masks in front of the Keck-I infrared secondary mirror. This technique converts the primary mirror into a VLA-style interferometric array, allowing the Fourier amplitudes and closure phases for a range of baselines to be recovered with minimal "redundancy" noise (e.g., Baldwin et al.

1986; Jennison 1958). For this work, we used both a non-redundant "Golay" mask and a circular "Annulus" mask; this information, along with observing dates, filter bandpasses, and calibrator sources, is included in Table 2. Aperture mask specifications, implementation description, and detailed observing methodology can be found in Tuthill et al. (2000b) and Monnier (1999).

For these observations the Near InfraRed-Camera (Matthews & Soifer 1994; Matthews et al. 1996) was used in a fast readout mode, adopting an integration time of 0.137 s per frame. Some of the data were corrupted by highly-variable seeing and "windshake," which blurs the fringes during the integration time and frustrates precise calibration. In situations where suspect calibration is indicated by our data pipeline diagnostics, previous (and/or subsequent) epochs of data have been included as a cross-check against possible faulty calibration. These individual situations are discussed on a case-by-case base later in the paper.

2.2. IOTA-FLUOR

Long-baseline observations described in this paper were carried out at the Infrared-Optical Telescope Array (IOTA), a Michelson stellar interferometer located on Mount Hopkins, Arizona (see Traub 1998, for a description of the IOTA instrument at the time of these observations). Observations were made in the near-IR K′ ($\lambda_0 = 2.16\mu m, \Delta\lambda = 0.32\mu m$) bands using three different IOTA configurations, with physical telescope separations between $B = 21$ m (North/South orientation) and 38 m (N-NE/S-SW orientation). For reference, the resolution corresponding to the longest baseline, as measured by the full-width at half maximum (FWHM) of the response to a point source, is $\lambda/2B = 6$ mas at K′.

The IOTA observations reported here (2000 February, April, June) were all carried out using the FLUOR beam combiner (Fiber Linked Unit for Optical Recombination, Coude Du Foresto et al. 1998) which uses single-mode fibers as spatial filters to achieve better precision in the measurement of fringe visibilities than achievable with bulk-optics combiners. A single-mode fiber essentially converts phase errors, caused by atmospheric turbulence and aberrated optics, into amplitude fluctuations which can be monitored and corrected (Shaklan & Roddier 1987; Shaklan 1989). In FLUOR, the light from each telescope is fed into a fluoride glass fiber and split into two parts. One part is directly sent to the detector as a monitor of the flux coupling efficiency ("photometric" signal), while the other is used for interference in a fiber coupler. By using the photometric signals, the fringe visibility can be precisely normalized for each measurement, thus calibrating effects of varying atmospheric turbulence. The fringes are modulated on the detector by a scanning piezo mirror placed in one leg of the interferometer, a fringe-detection scheme referred to as temporal modulation.

A typical single observation consisted of 200 scans obtained in ∼4 min, followed by calibration measurements of the background and single-telescope fluxes (important for characterizing the fiber coupler chromatic response). Target observations are interleaved with an identical sequence obtained on an unresolved or partially-resolved star, which serves to calibrate the interferometer's instrumental response and the effect of atmospheric seeing on the visibility amplitudes. The target and calibrator sources are typically separated on the sky by 5-10 degrees and are observed a few minutes apart; these conditions ensure that the calibrator observations provide a good estimate of the instrument's transfer function. The high brightness of our targets necessitated using similarly bright calibrators, which were partially resolved on the longest baselines. Uncertainty in the sizes of these calibrators dominate the calibration error in most cases, and we have compiled a list of the adopted angular diameters and sizes in Table 3.

3. Data Reduction

After briefly describing the basic data reduction procedures, we will present the results of validation experiments.

3.1. Keck Aperture Masking

The analysis procedures for extracting the visibility amplitudes and closure phases are well-documented in Tuthill et al. (2000b) and Monnier (1999). When performing image reconstructions, the Maximum Entropy Method (MEM) (Skilling & Bryan 1984; Gull & Skilling 1983) has been used to create diffraction-limited images from the interferometric data, as implemented in the VLBMEM package by Sivia (1987). Other engineering and performance details may be found in Tuthill et al. (2000b) and Monnier (1999), while other recent scientific applications of the data pipeline can be found in Monnier et al. (2002) and Tuthill et al. (2002).

3.2. IOTA-FLUOR

Reduction of the FLUOR data was carried out using custom software developed using the *Interactive Data Language* (IDL), similar in its main principles to that described by Coude Du Foresto et al. (1997). Significant efforts were made to validate the new data pipeline, and these are detailed in §3.4.

Here we briefly summarize the main steps in the data reduction procedure. We have included a more detailed description in Appendix A, including an explanation of our novel normalization scheme (§A.2). Our data pipeline includes data inspection, determination of a "kappa" matrix to characterize transfer function of fiber optics beam combiner, removal of photometric fluctuations, fringe amplitude normalization, power spectra measurement, calibration of instrumental response by observing calibrator stars, and standard data quality checks. Most targets were observed multiple times and the visibility measurements showed good internal consistency from night-to-night.

3.3. Systematic Errors

The most significant systematic errors in this experiment come from the aperture masking data at Keck (i.e., not from IOTA-FLUOR). In order to have reasonably-low read noise, limitations of the NIRC camera electronics restrict the integration time of each "speckle" frame to $\geq$0.137 s, many times longer than the typical atmospheric coherence time at 2.2μm ($\sim$40 ms). Even worse is "windshake" that occurs when observing low elevation sources into the wind, a common problem with large-aperture telescopes which results in a blurring of the fringes. Most damagingly, this can induce asymmetric mis-calibrations which must be carefully guarded against. Miscalibrations are usually identifiable in the raw data, thus allowing corrupted data to be flagged. In cases where we suspect problems (due to obvious windshake before or after the target), we have included previous/subsequent epochs of data as a cross-check, or have limited our analysis to the azimuthal-averages of the visibility data.

Fortunately, fringe-blurring problems have virtually no effect on the measurements of the closure phases, which remain well-calibrated and are crucial to the imaging process when the image is not centro-symmetric. In addition, the excellent Fourier coverage of the Keck masking allows hundreds of visibility points to be measured simultaneously, allowing averaging to recover high precision even when individual baselines show large fluctuations due to fringe-blurring (as long as due to statistical fluctuations of normal seeing – a systematic error occurs when wind-shake is present).

One common calibration difficulty encountered with the Keck aperture masking can be empirically corrected. When the coherence length r_0 or coherence time t_0 varies between observing the source and its calibrator, the overall ratio changes between the fringe power and the total flux on the detector. Fortunately for aperture masking data, this change is nearly constant as a function of baseline, for baselines longer than the coherence length ($\sim$0.5m at K band). In practice, this means the observed visibility function will approach a non-unity visibility at short baselines (e.g., $V_0 = 1.05$). As long as there is no significant

flux coming from large scales ($\sim$0.5″, a reasonable assumption at these wavelengths, but not strictly true due to scattering by dust), we can renormalize the visibility and recover reasonable data quality ($\lesssim$10% visibility errors on the longest baselines).

We have applied an empirical correction (simple scaling) for each epoch of aperture masking data before combining with IOTA data. An overall scaling of the visibility does not usually affect the image reconstruction process, but can here because we are combining the Keck data with IOTA-FLUOR results. We have chosen to apply this "correction" to all the Keck data rather than be selective; usually this correction is only a few percent, but is occasionally larger. Data will be presented both with and without this correction. The calibration factor was arrived at by fitting a Gaussian to the visibility data for baselines shorter than 1.5 m and using the derived y-intercept extrapolated to zero baseline.

In contrast to the relatively poor visibility calibration of the Keck aperture masking data, the IOTA-FLUOR experiment can produce visibility measurements with <1% precision, under some circumstances (Perrin et al. 1999; Perrin 2003). Achieving this precision requires control of many possible systematic errors, including corrections for chromaticity, detector non-linearities, and bandwidth-smearing. However, this level of precision is not necessary in this experiment for many reasons. First, the Keck aperture masking data typically suffers from greater (5-10%) calibration errors due to the effects discussed above, which fundamentally limits our analysis. Second, our sources have relatively low visibility fringes, meaning our IOTA measurements are photon-noise limited (or limited by knowledge of the calibrator stellar sizes) and not limited by systematic errors in most cases. Third, high-resolution structures in the dust shells are expected at the $\gtrsim$1% level, but can not be modelled/imaged without orders of magnitude more data; this acts as a kind of "noise" on the measurement which can not be expected to be fit by simple models.

As an aside, we expect it to be quite difficult to achieve 1% absolute precision for broadband fringe measurements when the source and calibrator have quite different spectra (as for dust-enshrouded targets); narrow-band filters and/or low-resolution spectroscopy should always be used for precision visibility measurements. Hence, while we do not claim <1% precision here, we do validate in the next section that our precision is $\lesssim$3% based on internal consistency checks and comparison with stars with previously measured diameters.

3.4. Validation

Tables 2 & 3 contain the observing and calibrator information for sources observed as part of our validation experiments, including RT Vir, R Leo, W Hya, and R Hya. Originally,

the last three were observed to measure the limb-darkening on these sources, but this has been deemed impossible due to the limitations in Keck calibration. However, because the limb-darkening effects are relatively subtle, these sources still serve to illustrate the calibration consistency and precision.

3.4.1. Internal consistency of IOTA-FLUOR visibilities

First, we validate the new IOTA-FLUOR data pipeline by showing visibility data of a single source at 3 different baselines. This range of baselines allows us to check the internal consistency of the data since the observations involved many configuration changes probing different resolutions. Figure 1 show the (u,v) coverage and visibility data for RT Vir. Although in general we will be showing averaged visibility data, here we present each individual visibility measurement (and error) in Figure 1b. In this panel, we also show the expected calibration errors based on the uncertainty in the calibrator diameters. In rare cases when the calibrator uncertainties are not significant, we have assumed a floor of 3% systematic error that might arise from unmodelled chromatic effects (based on software simulations of maximum miscalibrations possible from strong chromatic differences between source and calibrator using a model of the FLUOR coupler).

We have fit uniform disk models to this data and have separately calculated the statistical and systematic errors. Perrin (2003) presented a sophisticated analytical method for handling this situation in interferometry data analysis. An alternate method, employing bootstrap (Efron & Tibshirani 1993) and Monte Carlo sampling, is used here. For determining the statistical error, random subsets of averaged data (from each facility) are generated and a best-fit diameter is calculated for each case. Variance in the fit parameters directly yield the statistical errors and this method does not require assumptions concerning the noise distribution.

For the systematic errors, we have used a Monte Carlo method to vary the sizes of the calibrators used, given the uncertainties from Table 3. Usually systematic error slightly dominates over random error in this experiment, although neither affect the estimated sizes dramatically because the targets are generally heavily resolved. Note that all averaging occurs using the original V^2 and not the V in order to avoid bias for noisy datasets; however, we prefer to present our results using V (which is fully equivalent, since the errors are small after averaging).

The fit to the RT Vir data acts as a "Truth Test" for our data analysis pipeline. The visibility data span a range of 0.2 to 0.7, allowing a robust test of calibration. Figure 1c

shows the result of fitting a Uniform Disk (UD) to the dataset, both allowing the visibility at the origin (V_0) to float or be fixed to unity. For these two cases, we found the diameter to be $12.4 \pm 0.1 \pm 0.3$ and $12.6 \pm 0.1 \pm 0.4$ (the two error estimates are for statistical and systematic errors respectively, following standard convention). Most importantly, the reduced $\chi^2 \lesssim 1$ indicates a high level of internal consistency to the data calibration. Our measurement is similar to the second of the two diameters reported by Perrin (1996): 13.06±0.15 mas or 12.36±0.27 mas, depending on data selection (see Perrin thesis for more detailed discussion on this particular source).

When V_0 is not fixed to unity, a slightly better fit is found with $V_0 = 0.96$. This slight deviation from a perfect uniform disk could be due to many plausible mechanisms other than miscalibration, including changes in photospheric size between 2000Feb and 2000Apr, non-UD photospheric profile for this late-type star (M8III, semi-regular pulsator), or a small amount of scattered light from the known circumstellar dust shell (Hron et al. 1997). Regardless, we have shown an internal consistency <3% for our data pipeline. While the true internal calibration might be better than this, the data quality starts to be become limited by systematic errors.

3.4.2. Comparing Keck aperture masking and IOTA-FLUOR data

While most of our targets are complicated dust shell sources, a few "simple" sources can act to test the *relative* calibration between the Keck masking and IOTA-FLUOR data. This comparison is important since the the interferometry methods employed are clearly very different: Keck masking used image plane combination with narrow bandpass filters while IOTA used a fiber combiner over a broad wavelength band.

Figures 2-4 contain the (u,v) coverage and two-dimensional visibility from Keck aperture masking for R Leo, R Hya, and W Hya. The low declination of the latter two sources causes the 21 m physical baseline at IOTA to be projected to ∼11 m, thus providing a near-overlap with the 9 m longest baselines employed at Keck. This overlap regime allows another good check of the relative calibration procedures. The Keck masking data reveals these sources to be fairly circular, as expected. A separate calibrator study has shown that we expect 10-20% asymmetries from windshake and other systematic errors for sources of this size (Nick Murphy, private communication, 2003). Hence, any small residual asymmetries seen are likely to be miscalibrations and are not modelled here.

Figures 5-7 show the azimuthally-averaged data, both before and after applying the empirical Keck corrections described above in §3.3. Also, the results of the uniform disk fits

are shown, following the same procedure described above for RT Vir. The final results of UD diameter fits and relevant comments can be found in Table 4.

R Leo (Figure 5) shows a surprisingly good agreement at long and short baselines, completely consistent with a uniform disk with diameter 30.2±0.2±0.3 mas. This is contrary to recent findings of Perrin et al. (1999) who found strong evidence for deviations from uniform brightness, possibly due to (time-variable) molecular opacity effects (e.g., Mennesson et al. 2002; Jacob & Scholz 2002).

The shortest IOTA baselines and the longest Keck baselines are similar for R Hya and W Hya (Figure 6 & 7). Extrapolations of the Keck visibility show good agreement, at the ∼5-10% level, consistent with expected calibration errors of Keck data itself (additional data of HD 62623, VY CMa, and IRC +10420, presented in §4 also contain baseline near-overlaps and confirm this result). We conclude that any systematic errors resulting from the use of different filters at Keck and IOTA are less than other known sources of error.

R Hya and W Hya each show systematic deviations from a uniform disk profile shown in Figures 6 & 7, evident from the large reduced χ^2. While miscalibration could explain some of the changes, presence of dust emission and/or molecular layers in the upper atmosphere could also explain the discrepancies. Our use of different filter bandpasses for Keck and IOTA impacts our ability to study this effect, since molecular absorption dominate near the edges of the K band (Thompson et al. 2002) and are not probed by the Keck narrowband filters. Our observations highlight the need for more systematic study of Mira photospheres using narrow-band filters or spectroscopy.

Lastly, we consider a few miscellaneous effects which could affect the absolute data accuracy. For IOTA-FLUOR, calibration of the "effective" wavelength and corrections for bandwidth-smearing can be important for sources observed at and beyond the first null of the visibility pattern. In order to estimate the size of this first effect, we considered a simple model of the K′ filter and a reasonable range of effective temperatures, finding that the effective wavelength can only shift by ∼1%. Bandwidth-smearing destroys any true nulls in a visibility curve, because only a single wavelength experiences a null for a given projected baseline (thus non-nulled wavelengths dominate signal when using a broadband filter). For IOTA-FLUOR characteristics, the visibility minimum is V ∼2% at the location of the "Nulls" and the peaks are diminished by $\Delta V \sim 0.003$. This effect has been modelled for R Leo given the specific parameters of these new observations, and it was found not to significantly change the diameter estimation above.

3.5. Data quality summary

Given that these results represent the first use of IOTA-FLUOR data by our group and the first combination of it with Keck data, we have detailed the statistical and systematic errors encountered in a number of validation experiments. We have shown that the IOTA-FLUOR data pipeline is self-consistent with <3% precision in Visibility for the test observations of RT Vir. We find good agreement between visibilities measured at Keck and IOTA when using similar baselines on a common source, although detailed testing of this is currently limited by poor absolute calibration of Keck data at the longest baselines ($\sim$10%). These demonstrations are critical to give confidence in the fidelity of the results presented in the next section (and future papers which utilize these data), where challenges to data interpretation include large gaps in the baseline coverage and high uncertainties in the source models.

4. Results and discussion

In this section, we present the visibility data for six targets with resolved dust shells: HD 62623 (A3Iab), IRC +10420 (F8I), VY CMa (M3/4I), NML Cyg (M6I), VX Sgr (M4-9.5I), and IK Tau (M10III). The sources are at different states of stellar evolution and have a range of masses/luminosities. In this section, we discuss the data, modeling and imaging results for each source individually. Detailed modeling will be pursued in future papers using more sophisticated techniques.

In some cases, simple radiative transfer models were used to interpret the visibility data and to compare with previous results. We only consider spherically-symmetric models consisting of a central star (with radius R_* and effective temperature T_*) surrounded by a dust shell with a power-law density profile (usually $\rho \propto r^{-2}$, uniform outflow). The dust is assumed to begin at $R_{\rm inner}$ and extend to $R_{\rm outer}$. The dust shell optical depth was parameterized in terms of $\tau_{2.2\mu m}$. Additional details regarding the dust optical properties are given on a case-by-case basis below.

Figure 8 & 9 contain the (u,v) coverage of our observations. Most targets were observed on at least two IOTA baselines, and all have extensive visibility data for baselines shorter than 9 m from Keck aperture masking. The IOTA baselines tend to be oriented mostly N/S due to the geometry of the array. Because of this, low declination sources have relatively smaller (v)-components, reducing the attainable angular resolution.

4.1. "Peculiar" A2I supergiant HD 62623

The peculiar A2I supergiant HD 62623 has a significant IR excess recently modelled as due to the presence of circumstellar dust (Plets et al. 1995; Bittar et al. 2001). Bittar et al. (2001) used multi-wavelength Keck aperture masking data to constrain radiative transfer models of the putative dust shell. Here, we present additional Keck data and longer baseline IOTA data which confirm that the dust shell is indeed partially resolved.

No definitive signs of asymmetry were found in the 2-dimensional visibilities and closure phases of HD 62623 at 2.2μm for 3 different epochs. If the dust in this system is arranged in a circumbinary disk around the short-period ($\sim$137 days) binary in this system (binary separation is unresolved by the interferometer, major axis a $\lesssim 0.1$ AU ~ 0.14 mas at 700 pc, Plets et al. 1995), we conclude that the disk is viewed at a relatively low inclination (i.e., the disk is near face-on, if the disk geometry is valid).

Figure 10 shows the azimuthally averaged Keck masking data along with the longer baseline data from IOTA. The IOTA data is consistent with the Keck data and confirms that the dust shell is partially resolved. In order to further explore the consequences of these observations, we have generated a simple radiative transfer model that can fit the visibility data (included on Figure 10).

Our choice of stellar and dust shell parameters came mostly from the previous modeling work of Plets et al. (1995) and Bittar et al. (2001): $R_* = 0.33$ mas, $T_* = 9000$ K, $R_{\rm inner} = 8.3$ mas ($T_{\rm inner} = 1500$ K), $R_{\rm outer} = 1000 R_*$, $\rho \propto r^{-1.3}$ (Plets et al. 1995), $\tau_{2.2} = 0.16$, $a = 0.75\mu$m. Note that at a distance of 700 pc, this inner radius corresponds to 5.8 AU, much larger than the binary separation ($\lesssim$0.1 AU). For this modeling we used the publically-available radiative transfer code DUSTY (Ivezic et al. 1999), incorporating the (warm) silicate optical constants of Ossenkopf et al. (1992).

We emphasize that a large grain size ($a = 0.75\mu$m) was used in order to fit the visibility data (as found first by Bittar et al. 2001), otherwise the dust would be heated in excess of the expected sublimation temperature $T \sim 1500$K. While our model fits the visibility reasonably well, the dust does not produce enough infrared emission to match the observed SEDs (photometry extracted from Keck data yielded K mag 2.32$\pm$0.10, consistent with other recent IR photometry). Because the shell is optically thin, it is difficult to imagine a solution to this discrepancy, even if we abandon the assumption of spherical symmetry.

An alternate theory for the infrared excess was explored by Rovero & Ringuelet (1994), who found that it could be explained using only free-free/free-bound emission from a chromosphere without any dust. However, this model failed to explain the silicate feature seen in IRAS-LRS spectra (Plets et al. 1995). Further, the chromospheric models predict emission

arising within a few stellar radii of the photosphere (e.g., Lamers & Waters 1984), so close as to be unresolved by our interferometer observations.

The presence of near-infrared chromospheric emission, however, could help explain the inability of dust shell models to simultaneously fit the SED and near-IR visibility data. This extra emission would not be resolved but would contribute flux to the SED. Future observations with $\sim$10$\times$ greater resolution, such as with the CHARA Interferometer, can directly test this by resolving any chromospheric emission itself.

4.2. Rapidly-evolving F supergiant IRC+10420

IRC +10420 is an F supergiant, surrounded by a dust shell, thought to be caught in the short-lived phase of stellar evolution evolving from a red supergiant into a Wolf-Rayet star (Oudmaijer et al. 1996; Blöcker et al. 1999; Humphreys et al. 2002). The circumstellar envelope is known to be complex on large and small scales (Humphreys et al. 1997; Blöcker et al. 1999).

Figure 11 shows IOTA data and the azimuthally-averaged Keck visibility data. The emission from the dust shell ($\sim$38% of total K band flux) is resolved out on short baselines ($\lesssim$2m), and then there is a visibility plateau. As was the case for HD 62623, there are low-level asymmetries present in the Keck data (not shown) which we ascribe to residual miscalibration (the same asymmetry is not present in independent observations). Our results are consistent with similar observations at this wavelength published by Blöcker et al. (1999) for baselines $\lesssim$6m. The IOTA visibilities are slightly higher than the long-baseline Keck data, but consistent with our expected calibration (see §3.4).

The IOTA data extends our angular resolution of this system by a factor of $\sim$6 from previous observations. The fact that the visibility appears to remain constant from 9 m out to 36 m supports a model with an unresolved central source (diameter < 3 mas) containing $\sim$62% of the K-band flux; there is no evidence for a binary companion. We also note that photometry extracted from the Keck observations (K band: 3.63$\pm$0.10 mag) is consistent with the trend of decreasing brightness documented by Oudmaijer et al. (1996).

Under normal circumstances, we would attempt to fit the visibility data with a simple radiative transfer model to estimate physical parameters of the dust shell. However, for this source, Blöcker et al. (1999) has convincingly shown that the short-baseline visibility data can not be fit by a simple dust-shell model. Furthermore, complicated dust shell features are present in HST scattered light images by Humphreys et al. (1997), who argue that we are viewing a bipolar outflow from a near-polar direction, thus spherically symmetric modelling

is difficult to justify for this thick dust shell.

Modeling this system at the required level of sophistication is beyond the scope of this paper. We attempted to produce images of IRC +10420 using the aperture synthesis software (based on maximum entropy method). Unfortunately, mis-calibration in the Keck data corrupted the short baseline visibility (see §3.3). Since these short baselines are critical for reconstructing the large-scale structure present in this source, imaging must await better calibrated data.

4.3. Red Supergiant VY CMa

VY CMa is a red supergiant with extreme mass loss and high luminosity $> 10^5\,L_\odot$, approaching its end as a Type II supernova (see Monnier et al. 1999b, and references therein, for recent summary of the properties of this source). While the mid-infrared emission of the extensive dust shell around VY CMa can be fit by a spherically-symmetric outflow (Monnier et al. 2000a), the visible and near-infrared emission is dramatically asymmetric (Kastner & Weintraub 1998; Monnier et al. 1999b; Smith et al. 2001). Monnier et al. (1999b) used Keck aperture masking data to image the dust shell around this source at three infrared wavelengths. Here, we improve upon this work by incorporating the higher resolution IOTA data.

Figure 12 shows the 2-dimensional visibility data of VY CMa for Keck masking observations of 1999 February and 2000 January. Both datasets show striking asymmetric structure consistent with previous epochs. These data are azimuthally-averaged and included with the new IOTA data in Figure 13. The IOTA data allows the stellar component to be definitively separated from the dust component, and further yields a direct measurement of VY CMa's diameter. Firstly, we fit the diameter only using the IOTA data (result included in Table 4): 18.7±0.3±0.4 mas which contributes ∼36% of flux at 2.2μm. This is in reasonable agreement with a previous estimate of ∼20 mas assuming a $T_{\rm eff} \sim 2700$ (Monnier et al. 2000a; Le Sidaner & Le Bertre 1996). We emphasize that we measure an apparent diameter at this wavelength, and relation to the true "photospheric" diameter relies on additional assumptions of limb-darkening and other effects; late-type stars are known to have different apparent sizes between the visible, near-IR and mid-IR (Weiner et al. 2000).

We have modelled the dust shell using a spherically-symmetric radiative transfer model in order to illustrate how one can be misled by models when the true source structure is asymmetric and complex. The right-panel of Figure 13 shows the visibility curve of a model with the following parameters: $R_* = 9.35$ mas, $T_* = 2600$K, $R_{\rm inner} = 65$ mas

($T_{\rm inner} = 1050K$), $R_{\rm outer} = 5000\,{\rm mas}$, $\rho \propto r^{-2}$ (uniform outflow), $\tau_{2.2} = 2.18$. The effective temperature was found by fitting to the K band magnitude of VY CMa on 2000Jan26 of $+0.1\pm0.1$, based on photometry extracted from Keck data itself. Since we are using a simple blackbody function to estimate the stellar flux and because we are not fitting to the total luminosity, this temperature is not definitive (although the diameter measurement is direct). Assuming a distance of 1.5 kpc (Monnier et al. 1999b), the above angular quantities correspond to $R_* = 14\,{\rm AU}$ and $R_{\rm inner} = 97.5\,{\rm AU}$.

For this source, and the ones that follow, we have used the Wolfire radiative transfer code Wolfire & Cassinelli (1986) instead of DUSTY, which does not handle cases when the dust temperature is more than $\frac{1}{2}$ the photospheric temperature, as is often appropriate for the most evolved red giants and supergiants. Here we used warm silicate optical constants of Ossenkopf et al. (1992), with Mie scattering calculations based on Toon & Ackerman (1981), assuming MRN grain size distribution (Mathis et al. 1977). Details on use of this code have been given previously by Danchi et al. (1994) and Monnier et al. (1997).

As can be seen in Figure 13, the fit to the visibility data is reasonable at short and long baselines, but poor at intermediate scales. This fit could be improved by changing the assumed dust properties or adding another dust shell in order to modify the visibility curve. However in this case, unmistakably evidence in the closure phases and visibility amplitudes show that the deviation here comes from the fact that the dust shell is highly asymmetric. To better visualize the dust distribution, we have incorporated the high-resolution IOTA data into the image reconstruction process, although current software limitations (see §3.1) required an *ad hoc* approach. Figure 14 shows the image reconstruction results using the 1999 February masking data, with and without IOTA information. The left panel shows the image using only Keck data, and this epoch looks very similar to previous ones published by Monnier et al. (1999b).

When using Keck data only, the central source appears here to be slightly resolved and elongated (see left panel of Figure 14). While it is not impossible that the central star of VY CMa is highly elongated, it is more likely an artifact of the MEM algorithm (Narayan & Nityananda 1986) which attempts to spread out the light as much as possible consistent with the maximum spatial resolution of the data. In Figure 13 which incorporates IOTA data, we have shown that the central star contributes $\sim$36% of the K-band flux and is $\sim$18 mas in size. We can include this high-resolution information in the MEM fit by using the MEM prior, which is the default map that MEM uses when the data cannot constrain the solution. The technique of using the MEM prior to incorporate the presence of a compact central source known from either the SED or longer-baseline data, has already been explored by Monnier et al. (2003) and Tuthill et al. (2002); more discussion of this method can be found

in these references.

The right panel of Figure 14 shows the image reconstruction using a prior of an 18 mas star surrounded by asymmetric extended emission (based on previous imaging of Monnier et al. 1999b). While these two image reconstructions are very similar to each other (indeed, both fit the data with a reduced χ^2 $\sim$1), there are some details in the new image which are important. The dust distribution forms more of an arc to the south of the star and is less 'clumpy.' Without sufficient long-baseline (u,v) coverage, the MEM (or any other) method by itself can not precisely image dust very close to the stellar photosphere without the additional information of the stellar size and flux contribution.

Interpretation of this dust shell is complicated by its high optical depth. These new results confirm previous indications by Kastner & Weintraub (1998) and Monnier et al. (1999b) of bipolar dust distribution (the dusty "disk" is oriented roughly E/W). The K-band light arises predominantly from the southern "pole" of the dust envelope, where the relatively low optical depth allows hot dust emission near the star to be seen directly and also allows scattered light to escape into our line-of-sight. With high-fidelity images of this complicated dust shell, we can begin proper motions studies, as has already been demonstrated for IRC +10216 (Tuthill et al. 2000a). We hope to image new dust production episodes as they happen and to deduce the physics of mass-loss by following the time evolution of the circumstellar environment.

4.4. Red Supergiant NML Cyg

NML Cyg is an extreme red supergiant surrounded by an optically-thick dust envelope. Mid-infrared interferometry uncovered strong evidence for multiple shells of dust (Monnier et al. 1997). This basic result was confirmed and explored further by new near-infrared speckle measurements of Blöcker et al. (2001). Our new observations allow this dust shell to be imaged with unprecedented fidelity by separating the dust emssion from the stellar emission.

Figure 15 shows three separate Keck masking observations of NML Cyg. As was the case for VY CMa, the strong asymmetry is repeated in each independent measurement and thus can be reliably associated with source structure and not miscalibration. NML Cyg does not show large closure phases, indicating the emission is largely centro-symmetric (Monnier 2000), in marked contrast to VY CMa which showed large closure phases resulting from the highly asymmetric nebula (see Figure 14). Photometry from Keck found NML Cyg Kmag +0.55$\pm$0.10 at this epoch.

Figure 16 shows the azimuthally averaged Keck data along with limited IOTA measurements. The large gap between the two baseline ranges make interpolation uncertain. A uniform disk was fit to the longest-baseline Keck data and IOTA visibilities, and the result (diameter 7.8±0.4±0.5 mas) is shown in the right panel of this figure; this diameter estimate should be considered an upper limit until more extensive data fully characterizes the "knee" or "break" in the visibility curve between circumstellar and photospheric emission. Since the bolometric luminosity is well-constrained by the SED ($\sim$3.5 10^5 $L_\odot$at 1.8kpc, Monnier et al. 1997), this diameter implies $T_{\rm eff}$ $\sim$3650 K, somewhat hotter than expected for an M6 supergiant (e.g., $\sim$3375 K, van Belle et al. 1999).

Given the recent extensive efforts to model this dust shell, an overly-simplistic treatment here would serve little purpose. Instead, we present aperture synthesis images of the dust shell which allow us to discover asymmetries and clumpiness in a model-independent way.

We present image reconstructions following the strategy adopted in the last subsection for VY CMa. Figure 17 shows both image reconstruction with Keck masking data alone (left panel) and using a MEM prior to introduce the presence of an unresolved central source (with 59% of flux, based on IOTA data). In this case (unlike VY CMa earlier) the additional prior information has made a dramatic difference between these images. In the left panel, without the MEM prior containing the central source, the algorithm has created an image with a very elongated central source to fit the asymmetric visibility data. The size and shape of this central source is not physically plausible (i.e, a red supergiant photosphere is not expected to be this large and elongated), and thus we use a MEM prior to incorporate *a priori* information (derived from IOTA data) concerning the size and shape of the central source.

This example serves as a potent reminder that MEM imaging of extended dust shells around unresolved "point" sources depends greatly on the resolution of the interferometer *in the case that the dust shell is marginally resolved*. In this case, there is simply not enough information in the Keck data alone to constrain the large number of images consistent with the visibility data and closure phases. Indeed, both of these images fit the Keck data with a reduced χ^2 $\sim$1; it is the addition of *a priori* information regarding the nature of the stellar component that allows a higher fidelity image reconstruction.

The new image significantly advances our understanding of the NML Cyg dust shell by establishing that the inner circumstellar shell is not spherically symmetric. Astrophysically, the "Keck + IOTA" image can be understood in the context of the H_2O maser data of Richards et al. (1996), who found evidence already for a bipolar outflow along the NW/SE axis. We interpret our data as the first definitive detection of the dust asymmetry, showing an equatorial enhancement along the NE-SW axis, perpendicular to the maser outflow. This

identification could not have been made without combining the Keck with the IOTA data. The SiO maser data of Boboltz & Marvel (2000) has been interpreted as a sign of rotation about a NW-SE axis: it is interesting to speculate that the increased dust density seen in our image may be due to stellar rotation.

Bipolar outflows and the associated dust shell asymmetries are not reliably modelled with a spherically-symmetric radiative transfer code when the dust shell is optically thick. This can help explain the strong difficulty in fitting the near-IR visibility data at the same time as the SED and mid-IR visibility data (Monnier et al. 1997; Blöcker et al. 2001). The near-IR visibility is strongly affected by the fact that the average dust shell optical depth (which controls the total near-IR emission) is different to the line-of-sight optical depth (which affects the stellar contribution due to extinction). Assuming a different stellar fraction ($\neq 59\%$) causes the reconstructed dust shell to change somewhat in scale but not general morphology; additional data with resolution intermediate between Keck and this IOTA data will allow both the stellar diameter and fractional flux to be precisely measured. Until then, current conclusions should remain qualitative.

4.5. Red Supergiant VX Sgr

VX Sgr is a bright infrared source with strong maser emission, a red supergiant experiencing heavy mass loss. There has been no high-resolution near-IR data published since early speckle results of Dyck et al. (1984), when the dust shell was only partially resolved. Our new data has $\sim$5$\times$ greater resolution and the dust shell is easily resolved at short baselines ($\sim$3 m), allowing the dust and stellar components to be distinguished even without long baseline IOTA data. The two-dimensional visibility data from Keck show some evidence for asymmetry (i.e., deviations from circularity); however, since the dust contributes only $\sim$20% of the K-band flux, we can not place strong limits on possible asymmetries, given our calibration uncertainties. As was the case for NML Cyg previously, the closure phases for VX Sgr are all small ($\lesssim$3 degrees), indicating the dust shell is centro-symmetric.

Figure 18 shows the azimuthal-averages of the Keck data, along with extensive IOTA data allowing a diameter measurement of the underlying star. The most precise measurement comes by fitting to the IOTA data alone, which has sufficient baseline coverage to constrain the diameter 8.7$\pm$0.3$\pm$0.1 mas; this fit can be found in the figure. Also shown is a fit which includes the longest baseline Keck data: 9.5$\pm$0.2$\pm$1.0 mas. The latter estimate has a large systematic error due to known systematic errors in the Keck calibration at long baselines, however the two fits are statistically consistent. We conclude there is a 5% calibration difference between the IOTA and Keck datasets, although we can not determine the cause

(e.g., atmospheric miscalibration, filter bandpass differences).

Despite the calibration difficulties with the aperture masking which hampers measurements of asymmetries, the azimuthal averages of the three different masking datasets shown in Figure 18 are quite consistent with each other and motivates us to pursue radiative transfer modeling. Because the Keck data resolves the dust shell completely, we have performed modelling using this data set alone (without IOTA data explicitly, but using the angular diameter derived above), also incorporating the results of Keck photometry, K-band -0.2±0.1 mag. Figure 19 shows the reasonable fit for a simple model: $R_* = 4.35\,\mathrm{mas}$, $T_* = 3200\mathrm{K}$, $R_{\mathrm{inner}} = 60\,\mathrm{mas}$ ($T_{\mathrm{inner}} = 940K$), $R_{\mathrm{outer}} = 5000\,\mathrm{mas}$, $\rho \propto r^{-2}$ (uniform outflow), $\tau_{2.2} = 0.17$, and with dust properties and grain size distribution the same as described previously for VY CMa.

The diameter of VX Sgr found here is dramatically smaller than assumed in a recent modeling paper of Greenhill et al. (1995). In this paper, mid-IR interferometry from the ISI was used to constrain a radiative transfer model with a stellar diameter of 26 mas (3× larger than found here!). It is not clear why this previous model assumed such a large photosphere (and correspondingly low effective temperature) since the 10 micron visibility data did not have enough resolution to directly constrain the diameter as we do here. The SiO masers at ∼16.9 mas can now be interpreted to lie at 3.9 R_* (instead of 1.3 R_*) – a significant difference, showing that SiO masers do form well above the photosphere. We note that the dust shell parameters (which *were* constrained by the ISI mid-IR measurements) of Greenhill et al. (1995) are quite consistent with our current modeling of the near-IR Keck visibility data.

VX Sgr is a good source for future study, since the dust shell is fairly large and the high SNR closure phases from Keck show it to be centro-symmetric (recall that disk structures possess centro-symmetry, thus closure phases can not help in distinguishing circular dust shells from disks). In §4.7, we discuss some lessons learned regarding imaging dust shells around bright sources, such as VX Sgr.

4.6. O-rich Mira IK Tau

IK Tau is an evolved Mira variable star with an optically-thick, silicate-rich dust envelope. Here, we report the first high-resolution near-IR results since Dyck et al. (1984), extending full (u,v) coverage by a factor of ∼3. The Keck masking closure phases are small (close to zero), thus the dust shell appears centro-symmetric at this resolution (scales$\lesssim$50 mas). As for VX Sgr discussed earlier, the 2D visibility data from masking shows signs of asymmetries

which could not be confirmed due to poor data quality. Future observations will focus on the 2D visibilities, while we consider here only the azimuthally-averaged visibility in the context of model-fitting.

Figure 20 shows the azimuthally-averaged Keck data along with longer-baseline IOTA data. This combination allows the diameter of IK Tau to be measured for the first time. However, the large gap in baseline coverage between the longest Keck baselines and the IOTA baselines leaves some ambiguity for what data to use. One possibility is to fit a uniform disk to the IOTA data alone, which results in a diameter of 12.4±0.4±0.1 mas. There are two major problems with this result. First, this small size would require an effective temperature $\gtrsim$3000 K in order to have sufficient luminosity to match observed flux (based on Keck photometry, the K band magnitude of IK Tau on 2000Jan26 was -1.05±0.1). This is unlikely considering the strong CO and H_20 bands in the near-IR spectrum (Hyland et al. 1972), which suggests an $T_{\rm eff} \sim 2000K$ appropriate for a star with spectral type M10III. Furthermore, a simple radiative transfer model fit (not shown) with this small stellar component requires a dust shell inner radius of $R_{\rm in} \sim 10\,$mas, so close to the star that the dust would be heated to the unrealistically-high temperature of 2300 K.

Instead, we base our uniform disk fit on the baselines longer than 7 m and shorter than 21 m (ignoring the longest-baseline IOTA data at 27 m); the result of this fit appears in Figure 20. The fitted diameter, 20.2±0.2±0.3 mas, is more consistent with expectations, corresponding to an effective temperature of ∼2300 K. One major difficulty with this fit is that the prediction at the longest IOTA baseline (∼27 m) is not consistent with the measured data. Having dismissed the small 12.4 mas diameter that would be needed to fit both sets of IOTA data, we are left to explain this major discrepancy.

Our preferred explanation for the high visibility at the longest IOTA baselines is that the IK Tau photosphere has strong departures from uniform brightness, either due to hotspots (e.g., Tuthill et al. 1999a) or extended molecular emission (e.g., Tsuji et al. 1997; Matsuura et al. 2002; Jacob & Scholz 2002). Similar effects have already been seen around other late-type O-rich Miras (Perrin et al. 1999; Thompson et al. 2002). Given the extreme molecular band structures of M10III stars, this explanation takes on greater credence. Longer baseline data (preferable with closure phases) will be required to confirm this and to also rule out the presence of a binary companion.

A radiative transfer model has been fit to the visibility data using the 20.2 mas photospheric diameter, and satisfactory results were obtained. Figure 21 shows the predicted visibility curve at 2.2μm for a model with following parameters: $R_* = 10.1\,$mas, $T_* = 2300$K, $R_{\rm inner} = 35\,$mas ($T_{\rm inner} = 1100K$), $R_{\rm outer} = 5000\,$mas, $\rho \propto r^{-2}$ (uniform outflow), $\tau_{2.2} = 0.32$. We used the same dust properties as described previously for VY CMa. Assuming a distance

200 pc (Le Sidaner & Le Bertre 1996), then $R_* = 2.0\,\mathrm{AU}$ and $R_{\mathrm{inner}} = 7\,\mathrm{AU}$.

The longest baseline Keck data may not be fully resolving the dust shell, resulting in ambiguity over the fractional flux of the dust shell relative to the star. In order to explore the effects of this, we generated models with successively smaller stellar diameters. In order to maintain a reasonable fit, decreasing the stellar size requires increasing the dust contribution and decreasing the dust shell inner radius. Eventually, the inner radius becomes so small that an unphysical dust temperature is reached. In Figure 21, we have included the visibility curve for the most extreme model with plausible dust temperatures ($T_{\mathrm{inner}} = 1500K$): $R_* = 9.3\,\mathrm{mas}$, $T_* = 2500\mathrm{K}$, $R_{\mathrm{inner}} = 22\,\mathrm{mas}$, $\tau_{2.2} = 0.27$ (other parameters the same). This gives a marginally poorer fit to the Keck data (and short baseline IOTA data), supporting the previous model with the larger stellar diameter and cooler dust.

As for VX Sgr previously, we have not included a MEM image reconstruction here, due to the uncertainty in the stellar contribution and the limited observing set. Future observations with better calibrated visibilities and more uniform baseline coverage should allow high-fidelity imagery.

4.7. General comments on imaging with optical interferometers

In this paper, we successfully imaged only 2 of the 6 target stars with extended dust shells, VY CMa and NML Cyg; a lower success rate than anticipated. The imaging failures resulted for a variety of reasons, and we now discuss these in order to help other workers avoid the same pitfalls. While imaging work is only just beginning with optical interferometers, the proliferation of "imaging" arrays with three or more telescopes (COAST, NPOI, IOTA, ISI, CHARA, Keck, VLTI) presages impending expansion of imaging experiments; our experiences should prove instructive.

Images were made very early on with the Keck aperture masking experiment for the red supergiant VY CMa (Monnier et al. 1999b), dusty pinwheel nebulae around Wolf-Rayet stars (Tuthill et al. 1999b; Monnier et al. 1999a), carbon stars IRC +10216 and CIT 6 (Tuthill et al. 2000a; Monnier et al. 2000b), and young stars LkHα 101 and MWC 349 (Tuthill et al. 2000a; Danchi et al. 2001). Despite suffering from the same miscalibration problems encountered in this paper, imaging these sources was rather straightforward. Two major differences between these previously published sources and the sources presented here account for the differing ease of imaging: a) the dust shell dominated the flux (central source contributed little flux), and b) most of the previous dust shells were very asymmetric, possessing large non-zero closure phases. We now discuss the importance of each of these characteristics for imaging.

Consider a highly resolved dust shell with little or no contribution from an unresolved central source: the Visibility might be (say) 8% at some long baseline. Mis-calibrations are typically multiplicative and hence a 10% error corresponds to ΔV=0.008 at this baseline, a small fraction of the total dust shell contribution (fraction ∼1.0). However, consider the case when the dust shell only contributes 20% of the flux (as was the case for VX Sgr in this paper). This means that long-baseline visibility data (when the dust is mostly resolved and only the visibility from the central unresolved star is left) will be quite high, V∼80%. Hence, a 10% error translates to $\Delta V = 0.08$, quite significant effect considering the dust shell signal is at most only $\Delta V_{\rm shell} = 0.20$. Since the model for the central (point) source is well-known, this has the effect of essentially transferring *all* of the visibility error onto the remaining component – the dust shell.

From the examples above, you can see that for the same size dust shell, the signal-to-noise ratio of the dust shell visibilities ($\frac{\Delta V_{\rm shell}}{\Delta V_{\rm error}}$) go from $\frac{1.0}{0.008}$ ∼125 with no point source contribution to only $\frac{0.20}{0.08}$ ∼2.5 with an 80% point source, considering just multiplicative miscalibrations. Miscalibrations thus have a compounding effect when the central star dominates the flux (both the absolute level of miscalibration increases and the proportional effect compared to the dust shell signal increases). We remark that Albert Michelson, in the first interferometry experiments at Mt. Wilson (Michelson & Pease 1921), cleverly measured stellar diameters by finding the visibility null (V=0), which is zero no matter what the visibility miscalibration might be!

The second reason that imaging was easier with previous sources is because many are very asymmetric. The strong deviations from centro-symmetry meant that much of the morphology information was encoded in the Fourier phases and not just the Visibility amplitudes. This effect is enhanced for sources with strong central sources which dilute the closure phase signal of the dust shell. As discussed earlier in this work, the Keck masking experiment (and most interferometers) can measure closure phases quite accurately because atmospheric changes do not bias the measurement (e.g., Monnier 2000). In general, any image reconstruction procedure that incorporates a χ^2-type statistic to measure goodness-of-fit is most constrained by high signal-to-noise ratio (SNR) data. Hence the algorithm will implicitly rely heavily on the high SNR phase information when making images, and would be more immune to the miscalibrations in the visibility amplitudes. This is the main reason why imaging of VY CMa (Figure 14) showed fewer changes than NML Cyg (Figure 17) when long-baseline IOTA data was incorporated.

While the above problems affect optical interferometers more than radio interfometers, a third difficulty encountered for a few sources here is common to all interferometers: the Fourier coverage of the interferometer must match the angular size of the source being

observed. For IRC +10420, the dust shell is nearly too large for the Keck masking experiment (over-resolved on short baselines); for HD 62623, the baselines were not long enough to fully-resolve the dust shell structures.

In summary, imaging faint centro-symmetric dust shells around bright stars is difficult for reasons both obvious and subtle. *All of the effects* described above contributed to the problems encountered in this paper. The dust shells for most of the sources presented here contributed <50% of the flux and showed closure phase with only small departures from zero (the only major exception was VY CMa). Imaging these sources will remain challenging until excellent Fourier coverage and excellent visibility calibration (∼3% error) can be achieved at the same time.

An interesting consequence of the above difficulties is that there is a tendency to successfully image "strange-looking" dust shells, (e.g., VY CMa, CIT 6, IRC+10216), but to fail to easily image circularly-symmetric ones. This is consistent with the fact that the successfully-imaged sources (thus far) are not "normal" mass-losing stars, but rather are extreme cases that were most suitable for early interferometric imaging. Although current evidence suggests that large-scale dust shell asymmetries are common to mass-losing stars, too few dust shells have been imaged to say this with confidence. As the spatial resolution and sensitivity of interferometers improves, we should be able to image more "normal" evolved stars and begin to know whether strange dust shells are the exception or the rule.

5. Conclusions

Major results here fall into two categories: stellar diameters and circumstellar dust shells.

We were able to measure 2.2μm stellar sizes of a number of dust-obscured sources for the first time. The VX Sgr diameter was found to be about 3× smaller than previous modeling, with important repercussions for understanding the SiO maser distribution. The IK Tau and NML Cyg data suggest either photospheric profiles that strongly deviate from a uniform disk or the presence of an extra component to the system that is not being modelled here (e.g., a binary companion). Long-baseline (>20m) data with closure-phase arrays are needed to understand this better.

These diameter measurements allowed the stellar and dust contributions to be separated in most cases. By increasing the angular resolution in the near-IR by 3-10× over best current literature measurements, our new data offer strong constraints for new radiative transfer modeling. In addition, the dust shells for a few sources were imaged using maximum

entropy method. When assisted by a MEM prior incorporating the long-baseline IOTA data, dust shell asymmetries and clumpiness are unambiguously identified and separated from photospheric light. Unfortunately, we were only able to confidently make images for a subset of these sources, due to problems with calibration of the atmospheric transfer function in the aperture masking experiment and to incomplete sampling at longer baselines; however, these limited results have proved enlightening. Most importantly, we have found a bipolar dust shell geometry for NML Cyg, as earlier suggested by OH, H_2O, and SiO masers, giving credence to some alternative mass-loss mechanisms (e.g., involving magnetic fields and/or rotation).

While it lies beyond of the scope of this paper, future detailed modeling of the data presented here will dramatically improve our knowledge of these sources and our results point the way toward new classes of dust shell models. It has lately been fashionable to extend spherically-symmetric radiative transfer modeling up to (or beyond) the range of applicability, by incorporating multiple dust shells and unusual dust properties to fit multi-wavelength dust shell observations. When viewed together with other recent aperture masking results (see Figure 22), the new images presented here strengthen the argument that clumpiness and global asymmetry should be considered more seriously as the main explanation for the observed deviations from simple uniform-outflow models. We suggest that *global* dust shell properties are best derived from mid-IR observations where dust emission dominates over stellar and the effects of clumpiness are better "averaged-out" by the intrinsically larger emission volume in the mid-IR. Presumably, the larger emission volume will encompass many such "clumps" as well as a longer span of mass-loss history, and should represent average dust shell properties more faithfully.

We have also showed examples of how MEM imaging of interferometry data can yield very different dust shell images, depending on the MEM prior being used, and have discussed the difficulties in imaging faint dust shells around bright stars. We recognize and emphasize that optical interferometry is still at an early stage of development, and recent image reconstructions can not be interpreted as straightforwardly as those derived from the Very Large Array (VLA) or other radio interferometers. The use of *a priori* information is critical for accurately interpreting data from marginally resolved sources, and new imaging software is needed to facilitate this (the method used here was admittedly *ad hoc*). All the visibility data here (Keck masking and IOTA) have been converted to the new FITS format for Optical Interferometry data (OI-FITS) [1] and are available upon request.

[1]http://www.mrao.cam.ac.uk/ jsy1001/exchange/

Results from the IOTA interferometer would not have been possible without continued support from the Smithsonian Astrophysical Observatory. This research has made use of the SIMBAD database, operated at CDS, Strasbourg, France, and NASA's Astrophysics Data System Abstract Service. Some data presented herein were obtained at the W.M. Keck Observatory, which is operated as a scientific partnership among the California Institute of Technology, the University of California and the National Aeronautics and Space Administration. The Keck Observatory was made possible by the generous financial support of the W.M. Keck Foundation. The *getCal* program is a product of the Michelson Science Center (IPAC, Caltech).

A. IOTA-FLUOR Data Reduction Details

A.1. Basic procedures

Reduction of the FLUOR data was carried out using custom software developed using the *Interactive Data Language* (IDL), similar in its main principles to that described by Coude Du Foresto et al. (1997).

The major steps of the data reductions are:

1. Data inspection. The raw fringe data is background-subtracted and inspected. Cosmic ray hits and other detector anomalies are automatically detected and removed. Visual inspection of the power spectra allow for flagging of data corrupted by instrumental problems, in particular delay line vibrations. Although troublesome, these problems are easily identified and removed from the data stream.

2. "Kappa" matrix. Coude Du Foresto et al. (1997) described the use of the kappa matrix for removal of photometric fluctuations and normalization of the fringe amplitudes. The kappa matrix is chromatic and thus must be measured separately for each source and calibrator. Stability of the kappa matrix during the night is a useful diagnostic of data quality.

3. Removal of photometric fluctuations. During poor seeing, rapid coupling fluctuations will contain high-frequency power which mimic real fringes. The interferometric channels have the incoherent part of the flux removed using the photometric signals and the kappa matrix, which eliminates scintillation and coupling fluctuations (a strong effect).

4. Fringe normalization. In each scan, the expected fringe envelope for 100% coherent

light (unity visibility) is calculated from the photometric and kappa measurements (e.g., Coude Du Foresto et al. 1997), which allows for precise calibration of the observed fringe visibility independent of the atmosphere. Coude Du Foresto et al. (1997) advocate dividing the fringe data by the envelope at this stage, however we have pursued a different strategy which is more robust for low light levels and is described in the next section of the appendix.

5. Power Spectra Measurement. Next the power spectra are calculated for each scan. Noise sources cause a bias in the power spectrum which must be removed. The contribution from read noise is estimated from calibration measurements of dark sky, while the remaining bias (from photon noise and uncorrected scintillation) is estimated by measuring the power at frequencies both above and below the fringe frequency and interpolating for the intermediate (fringe) frequencies; this bias term is subtracted for each scan. For the classical FLUOR analysis from Coude Du Foresto et al. (1997), this "power" is directly proportional the V^2 (Squared-Visibility) and can be averaged. In our method, we combine this measurement with the normalization factor appropriate for that scan, and make a weighted average of the normalized scans using bootstrap sampling (Efron & Tibshirani 1993).

6. Instrumental Response. The above procedure is repeated for the target and calibrator stars. After correction for finite size effects, the calibrator V^2 are used to monitor the instrumental transfer function as a function of time. Using simple linear interpolation to estimate the transfer function at the times the target observations were made, we divide the target V^2 by the interpolated calibrator V^2 to yield a final calibrated measurement of V^2.

7. Standard data quality checks. We always analyze the two interferometric channels independently and also apply both the classical FLUOR method and our new normalization scheme in parallel. Our results from the the two methods, and for both fringe outputs, are statistically and internally consistent for bright sources.

A.2. Normalization Scheme

Here, we describe more quantitatively the novel normalization procedure used in the IOTA-FLUOR data reduction.

The method of dividing by the fringe envelope, as described in detail by Coude Du Foresto et al. (1997), does correct for the varying photometric signal strengths, but amplifies noise when the signals are small. For bright sources, signals are never small and thus this

limitation poses no problem; in fact, dividing by the envelope (sample-by-sample) maximizes the precision of observations when limited by calibration of coupling fluctuations (i.e., when you are not limited by detector read-noise or photon-noise). However in the experiment reported here, we observed low visibility sources which had a signal-to-noise ratio (in a single scan) which was sometimes below the threshold used by traditional FLUOR analysis (SNR$\sim$3).

In our method, we measure an average normalization for each scan based on the photometric signal. Hence, rather than treating each scan equally when taking the power spectrum, we have assigned a normalization that is used to both weight the average power spectrum and also allows the weighting to be done in a statistical way that is free of bias. Here we briefly describe the method (see Coude Du Foresto et al. 1997; Monnier 2001, for more background on the notation and related methods).

As already mentioned, the incoherent flux that appears on the interferometric channels (I1, I2) is a linear combination of the signals that appear on the photometric channels (P1, P2); the kappa matrix can be used then to "predict" (I1,I2) given (P1,P2). In addition, we can use the components of the kappa matrix to predict the maximum amplitude of the coherent part of the interferometric channels. This can written as:

$$I_1 = \kappa_{(P_1,I_1)} P_1 + \kappa_{(P_2,I_1)} P_2 + 2\sqrt{\kappa_{(P_1,I_1)} P_1 \kappa_{(P_2,I_1)} P_2} \cdot \gamma(t) \tag{A1}$$

Here, $\gamma(t)$ is the mutual coherence function and encodes the fringe visibility, the quantity we wish to measure. Usually γ is temporally modulated by adjusting the relative path lengths in the two arms of the interferometer. An equation for I_2 follows from the above. Hence, for perfect coherence $\|\gamma\|$=1, the maximum measured fringe amplitude would be (*not* normalized by mean flux):

$$I_1^{\text{envelope}} = 2\sqrt{\kappa_{(P_1,I_1)} P_1 \kappa_{(P_2,I_1)} P_2} \tag{A2}$$

In the power spectrum method, the V^2 is measured because it is free of bias from read noise and photon noise. Applying Parseval's Theorem to the coherent part of the fringe interferogram, we can understand this integration of the fringe "power" in the Fourier (frequency) Space as equivalent to the integration of the square of the fringe envelope in time. Hence, we intend to normalize the measured fringe "power" by the average of:

$$(I_1^{\text{envelope}})^2 = 4\kappa_{(P_1,I_1)} \kappa_{(P_2,I_1)} P_1 P_2 \tag{A3}$$

Figure 23 shows an example of this method applied to one interferometric output of a single observation set of a bright source (σ CMa). This figure shows that the (bias-corrected)

fringe power varies by a large amount due to coupling fluctuations but that our "normalization" factor, calculated from the photometric channels, faithfully tracks this variation. We can also see the fringe power is very linear with normalization and a simple weighted-mean is used to estimate the slope of the relation, a value proportional to V^2. In this example, the error was calculated using a bootstrap method and the 1.3% uncertainty in the slope is reflected in the plot.

Typically, one might worry that Poisson and read noise would bias the above normalization. However, one can see that this quantity is not biased as long as P_1 and P_2 are uncorrelated on the timescale of single scan ($<<$ 1 sec), a reasonable assumption for a long-baseline interferometer where the atmospheric distortion above an aperture is independent of the others. Note, that this useful statistical property also implies that one could also average P_1 and P_2 separately, as pointed out by Shaklan et al. (1992), and still have a good bias-free estimate of the fringe amplitude normalization.

REFERENCES

Akeson, R. L., Ciardi, D. R., van Belle, G. T., & Creech-Eakman, M. J. 2002, ApJ, 566, 1124

Akeson, R. L., Ciardi, D. R., van Belle, G. T., Creech-Eakman, M. J., & Lada, E. A. 2000, ApJ, 543, 313

Baldwin, J. E., Haniff, C. A., Mackay, C. D., & Warner, P. J. 1986, Nature, 320, 595

Bittar, J., Tuthill, P., Monnier, J. D., Lopez, B., Danchi, W., & Stee, P. 2001, A&A, 368, 197

Blöcker, T., Balega, Y., Hofmann, K.-H., Lichtenthäler, J., Osterbart, R., & Weigelt, G. 1999, A&A, 348, 805

Blöcker, T., Balega, Y., Hofmann, K.-H., & Weigelt, G. 2001, A&A, 369, 142

Boboltz, D. A. & Marvel, K. B. 2000, ApJ, 545, L149

Chiang, E. I. & Goldreich, P. 1997, ApJ, 490, 368

Colavita, M., Akeson, R., Wizinowich, P., Shao, M., Acton, S., Beletic, J., Bell, J., Berlin, J., Boden, A., Booth, A., Boutell, R., Chaffee, F., Chan, D., Chock, J., Cohen, R., Crawford, S., Creech-Eakman, M., Eychaner, G., Felizardo, C., Gathright, J., Hardy, G., Henderson, H., Herstein, J., Hess, M., Hovland, E., Hrynevych, M., Johnson, R.,

Kelley, J., Kendrick, R., Koresko, C., Kurpis, P., Le Mignant, D., Lewis, H., Ligon, E., Lupton, W., McBride, D., Mennesson, B., Millan-Gabet, R., Monnier, J., Moore, J., Nance, C., Neyman, C., Niessner, A., Palmer, D., Reder, L., Rudeen, A., Saloga, T., Sargent, A., Serabyn, E., Smythe, R., Stomski, P., Summers, K., Swain, M., Swanson, P., Thompson, R., Tsubota, K., Tumminello, A., van Belle, G., Vasisht, G., Vause, J., Walker, J., Wallace, K., & Wehmeier, U. 2003, ApJ, 592, L83

Coude Du Foresto, V., Perrin, G., Ruilier, C., Mennesson, B. P., Traub, W. A., & Lacasse, M. G. 1998, in Proc. SPIE Vol. 3350, p. 856-863, Astronomical Interferometry, Robert D. Reasenberg; Ed., 856–863

Coude Du Foresto, V., Ridgway, S., & Mariotti, J.-M. 1997, A&AS, 121, 379

Danchi, W. C., Bester, M., Degiacomi, C. G., Greenhill, L. J., & Townes, C. H. 1994, AJ, 107, 1469

Danchi, W. C., Tuthill, P. G., & Monnier, J. D. 2001, ApJ, 562, 440

Dyck, H. M., Zuckerman, B., Leinert, C., & Beckwith, S. 1984, ApJ, 287, 801

Efron, B. & Tibshirani, R. J. 1993, An introduction to the bootstrap (New York: Chapman and Hall)

Gauger, A., Balega, Y. Y., Irrgang, P., Osterbart, R., & Weigelt, G. 1999, A&A, 346, 505

Greenhill, L. J., Colomer, F., Moran, J. M., Backer, D. C., Danchi, W. C., & Bester, M. 1995, ApJ, 449, 365+

Gull, S. F. & Skilling, J. 1983, in Indirect Imaging. Measurement and Processing for Indirect Imaging. Proceedings of an International Symposium held in Sydney, Australia, August 30-September 2, 1983. Editor, J.A. Roberts; Publisher, Cambridge University Press, Cambridge, England, New York, NY, 1984. LC # QB51.3.E43 I53 1984. ISBN # 0-521-26282-8. P.267, 1983, 267+

Habing, H. J. 1996, A&A Rev., 7, 97

Hale, D. D. S., Bester, M., Danchi, W. C., Hoss, S., Lipman, E., Monnier, J. D., Tuthill, P. G., Townes, C. H., Johnson, M., Lopez, B., & Geballe, T. R. 1997, ApJ, 490, 407

Haniff, C. A. & Buscher, D. F. 1998, A&A, 334, L5

Hartmann, L., Kenyon, S. J., & Calvet, N. 1993, ApJ, 407, 219

Hearn, A. G. 1990, in From Miras to Planetary Nebulae: Which Path for Stellar Evolution?, 121–130

Heras, A. M., Shipman, R. F., Price, S. D., de Graauw, T., Walker, H. J., Jourdain de Muizon, M., Kessler, M. F., Prusti, T., Decin, L., Vandenbussche, B., & Waters, L. B. F. M. 2002, A&A, 394, 539

Hillenbrand, L. A., Strom, S. E., Vrba, F. J., & Keene, J. 1992, ApJ, 397, 613

Hofmann, K.-H., Balega, Y., Blöcker, T., & Weigelt, G. 2001, A&A, 379, 529

Hron, J., Aringer, B., & Kerschbaum, F. 1997, A&A, 322, 280

Humphreys, R. M., Davidson, K., & Smith, N. 2002, AJ, 124, 1026

Humphreys, R. M., Smith, N., Davidson, K., Jones, T. J., Gehrz, R. T., Mason, C. G., Hayward, T. L., Houck, J. R., & Krautter, J. 1997, AJ, 114, 2778

Hyland, A. R., Becklin, E. E., Frogel, J. A., & Neugebauer, G. 1972, A&A, 16, 204

Ivezic, Z. & Elitzur, M. 1996a, MNRAS, 279, 1019

—. 1996b, MNRAS, 279, 1011

Ivezic, Z., Nenkova, M., & Elitzur, M. 1999, User Manual for DUSTY, Tech. rep., University of Kentucky

Jacob, A. P. & Scholz, M. 2002, MNRAS, 336, 1377

Jennison, R. C. 1958, MNRAS, 118, 276+

Kastner, J. H. & Weintraub, D. A. 1998, AJ, 115, 1592

Lafon, J. P. J. & Berruyer, N. 1991, A&A Rev., 2, 249

Lamers, H. J. G. L. M. & Waters, L. B. F. M. 1984, A&A, 136, 37

Le Sidaner, P. & Le Bertre, T. 1996, A&A, 314, 896

Lopez, B., Danchi, W. C., Bester, M., Hale, D. D. S., Lipman, E. A., Monnier, J. D., Tuthill, P. G., Townes, C. H., Degiacomi, C. G., Geballe, T. R., Greenhill, L. J., Cruzalebes, P., Lefevre, J., Mekarina, D., Mattei, J. A., Nishimoto, D., & Kervin, P. W. 1997, ApJ, 488, 807

Mathis, J. S., Rumpl, W., & Nordsieck, K. H. 1977, ApJ, 217, 425

Matsuura, M., Yamamura, I., Cami, J., Onaka, T., & Murakami, H. 2002, A&A, 383, 972

Matthews, K., Ghez, A. M., Weinberger, A. J., & Neugebauer, G. 1996, PASP, 108, 615+

Matthews, K. & Soifer, B. T. 1994, Infrared Astronomy with Arrays: the Next Generation, I. (Dordrecht: Kluwer Academic Publishers), 239

Mennesson, B., Perrin, G., Chagnon, G., Foresto, V. C. d., Ridgway, S., Merand, A., Salome, P., Borde, P., Cotton, W., Morel, S., Kervella, P., Traub, W., & Lacasse, M. 2002, ApJ, 579, 446

Michelson, A. A. & Pease, F. G. 1921, ApJ, 53, 249

Millan-Gabet, R., Schloerb, F. P., & Traub, W. A. 2001, ApJ, 546, 358

Millan-Gabet, R., Schloerb, F. P., Traub, W. A., Malbet, F., Berger, J. P., & Bregman, J. D. 1999, ApJ, 513, L131

Monnier, J. D. 1999, PhD thesis, University of California at Berkeley

Monnier, J. D. 2000, in Principles of Long Baseline Stellar Interferometry, 203–+

—. 2001, PASP, 113, 639

Monnier, J. D., Bester, M., Danchi, W. C., Johnson, M. A., Lipman, E. A., Townes, C. H., Tuthill, P. G., Geballe, T. R., Nishimoto, D., & Kervin, P. W. 1997, ApJ, 481, 420

Monnier, J. D., Danchi, W. C., Hale, D. S., Lipman, E. A., Tuthill, P. G., & Townes, C. H. 2000a, ApJ, 543, 861

Monnier, J. D. & Millan-Gabet, R. 2002, ApJ, 579, 694

Monnier, J. D., Millan-Gabet, R., Tuthill, P. G., Traub, W. A., Carleton, N. P., Coude du Foresto, V., Danchi, W. C., Lacasse, M. G., Morel, S., Perrin, G. S., & Porro, I. L. 2003, in Interferometry for Optical Astronomy II. Edited by Wesley A. Traub. Proceedings of the SPIE, Volume 4838, pp. 379-386 (2003)., 379–386

Monnier, J. D., Tuthill, P. G., & Danchi, W. C. 1999a, ApJ, 525, L97

—. 2000b, ApJ, 545, 957

—. 2002, ApJ, 567, L137

Monnier, J. D., Tuthill, P. G., Lopez, B., Cruzalebes, P., Danchi, W. C., & Haniff, C. A. 1999b, ApJ, 512, 351

Narayan, R. & Nityananda, R. 1986, ARA&A, 24, 127

Ossenkopf, V., Henning, T., & Mathis, J. S. 1992, A&A, 261, 567

Oudmaijer, R. D., Groenewegen, M. A. T., Matthews, H. E., Blommaert, J. A. D. L., & Sahu, K. C. 1996, MNRAS, 280, 1062

Pasinetti-Fracassini, L. E., Pastori, L., Covino, S., & Pozzi, A. 2001, A&A, 367, 521

Perrin, G. 1996, PhD thesis, L'Université de Paris

—. 2003, A&A, 400, 1173

Perrin, G., Coudé du Foresto, V., Ridgway, S. T., Mennesson, B., Ruilier, C., Mariotti, J.-M., Traub, W. A., & Lacasse, M. G. 1999, A&A, 345, 221

Plets, H., Waelkens, C., & Trams, N. R. 1995, A&A, 293, 363

Richards, A. M. S., Yates, J. A., & Cohen, R. J. 1996, MNRAS, 282, 665

Richichi, A. & Percheron, I. 2002, A&A, 386, 492

Rovero, A. C. & Ringuelet, A. E. 1994, MNRAS, 266, 203

Rowan-Robinson, M. & Harris, S. 1982, MNRAS, 200, 197

Shaklan, S. B. 1989, Ph.D. Thesis

Shaklan, S. B., Colavita, M. M., & Shao, M. 1992, in High-Resolution Imaging by Interferometry, 1287–+

Shaklan, S. B. & Roddier, F. 1987, Appl. Opt., 26, 2159

Sivia, D. 1987, PhD thesis, Cambridge University

Skilling, J. & Bryan, R. K. 1984, MNRAS, 211, 111+

Smith, N., Humphreys, R. M., Davidson, K., Gehrz, R. D., Schuster, M. T., & Krautter, J. 2001, AJ, 121, 1111

Thompson, R. R., Creech-Eakman, M. J., & van Belle, G. T. 2002, ApJ, 577, 447

Toon & Ackerman. 1981, Appl. Opt., 20, 3657

Traub, W. A. 1998, in Proc. SPIE Vol. 3350, p. 848-855, Astronomical Interferometry, Robert D. Reasenberg; Ed., 848–855

Tsuji, T., Ohnaka, K., Aoki, W., & Yamamura, I. 1997, A&A, 320, L1

Tuthill, P. G., Haniff, C. A., & Baldwin, J. E. 1999a, MNRAS, 306, 353

Tuthill, P. G., Monnier, J. D., & Danchi, W. C. 1999b, Nature, 398, 487

—. 2001, Nature, 409, 1012

Tuthill, P. G., Monnier, J. D., Danchi, W. C., Hale, D. D. S., & Townes, C. H. 2002, ApJ, 577, 826

Tuthill, P. G., Monnier, J. D., Danchi, W. C., & Lopez, B. 2000a, ApJ, 543, 284

Tuthill, P. G., Monnier, J. D., Danchi, W. C., Wishnow, E. H., & Haniff, C. A. 2000b, PASP, 112, 555

van Belle, G. T., Lane, B. F., Thompson, R. R., Boden, A. F., Colavita, M. M., Dumont, P. J., Mobley, D. W., Palmer, D., Shao, M., Vasisht, G. X., Wallace, J. K., Creech-Eakman, M. J., Koresko, C. D., Kulkarni, S. R., Pan, X. P., & Gubler, J. 1999, AJ, 117, 521

Weigelt, G., Balega, Y., Bloecker, T., Fleischer, A. J., Osterbart, R., & Winters, J. M. 1998, A&A, 333, L51

Weigelt, G., Balega, Y. Y., Blöcker, T., Hofmann, K.-H., Men'shchikov, A. B., & Winters, J. M. 2002, A&A, 392, 131

Weiner, J., Danchi, W. C., Hale, D. D. S., McMahon, J., Townes, C. H., Monnier, J. D., & Tuthill, P. G. 2000, ApJ, 544, 1097

Wittkowski, M., Langer, N., & Weigelt, G. 1998, A&A, 340, L39

Wolfire, M. G. & Cassinelli, J. P. 1986, ApJ, 310, 207

Table 1. Basic Properties of Targets

Target Name	RA (J2000)	Dec (J2000)	V mag[a]	K mag[a]	Spectral Type	Type of Source
IK Tau	03 53 28.84	+11 24 22.6	11.9	-1.1	M10III	Dust-enshrouded Mira variable
VY CMa	07 22 58.33	−25 46 03.2	8.0	+0.1	M3/4I	Dust-enshrouded red supergiant
HD 62623	07 43 48.47	−28 57 17.4	4.0	2.3	A3Iab	A supergiant with infrared excess
R Leo	09 47 33.49	+11 25 43.6	6.0	-2.2	M8III	Mira variable
RT Vir	13 02 37.98	+05 11 08.4	8.6	-1.0	M8III	Semi-regular variable
R Hya	13 29 42.78	−23 16 52.8	6.4	-2.6	M7III	Mira variable
W Hya	13 49 01.00	−28 22 03.5	7.5	-3.1	M7III	Mira variable
VX Sgr	18 08 04.05	−22 13 26.6	10.0	0.2	M4-9.5I	Dust-enshrouded red superigant
IRC +10420	19 26 48.03	+11 21 16.7	8.5	3.6	F8I	Rapidly-evolving F supergiant
NML Cyg	20 46 25.46	+40 06 59.6	16.6	0.6	M6I	Dust-enshrouded red supergiant

[a]Most of the targets are variable stars and these magnitudes are merely representative. See text for mor recent photometry.

Table 2. Journal of Observations

Target (Sp. Type)	Date (UT)	λ (μm)	$\Delta\lambda$ (μm)	Interferometer Configuration	Calibrator Names
HD 62623	1999Apr26	2.269	0.155	Keck Annulus	HD 47667
(A3Iab)	2000Jan26	2.269	0.155	Keck Annulus	54 Per
	2000Feb05,07	2.16	0.32	IOTA N15-S15	HD 63852
	2000Feb10	2.16	0.32	IOTA N25-S15	HD 63852
IK Tau	2000Jan26	2.257	0.053	Keck Golay 21	α Cet
(M10III)	2000Feb03,05,07	2.16	0.32	IOTA N15-S15	o Tau
	2000Feb08,10	2.16	0.32	IOTA N25-S15	o Tau
IRC +10420	2000Jun16,17	2.16	0.32	IOTA N35-S15	SAO 104467
(F8I)	2000Jun24	2.269	0.155	Keck Annulus	SAO 104655,SAO 104467
NML Cyg	2000Jun23	2.16	0.32	IOTA N35-S15	SAO 49410
(M6I)	2000Jun24	2.257	0.053	Keck Annulus	ξ Cyg
	2000Jun24	2.257	0.053	Keck Golay 21	SAO 105500
	2000Jun24	2.269	0.155	Keck Golay 21	ξ Cyg
R Hya	2000Jan26	2.257	0.053	Keck Golay 21	δ Vir, 2 Cen, π Leo, SW Vir
(M7III)	2000Feb04,05	2.16	0.32	IOTA N15-S15	γ Hya
	2000Feb08,09	2.16	0.32	IOTA N25-S15	γ Hya
R Leo	2000Jan26	2.257	0.053	Keck Golay 21	π Leo
(M8III)	2000Feb01,05,06	2.16	0.32	IOTA N15-S15	π Leo
RT Vir	2000Feb03,05	2.16	0.32	IOTA N15-S15	σ Vir
(M8III)	2000Apr12,13,15	2.16	0.32	IOTA N35-S15	σ Vir
	2000Apr20	2.16	0.32	IOTA N25-S15	σ Vir
VX Sgr	2000Apr12,13,14,20	2.16	0.32	IOTA N35-S15	SAO 186841
(M4-9.5I)	2000Apr23	2.16	0.32	IOTA N25-S15	SAO 186841
	2000Jun21	2.16	0.32	IOTA N35-S15	SAO 186841
	2000Jun24	2.249	0.024	Keck Annulus	14 Sgr
	2000Jun24	2.257	0.053	Keck Golay 21	SAO 186681, SAO 186841
W Hya	2000Jan26	2.249	0.024	Keck Golay 21	2 Cen
(M7III)	2000Feb04,05,06	2.16	0.32	IOTA N15-S15	π Hya
VY CMa	1999Feb05	2.257	0.053	Keck Golay 21	σ CMa
(M3/4I)	2000Jan26	2.269	0.155	Keck Annulus	54 Per, π Leo, σ CMa
	2000Feb04,05,07	2.16	0.32	IOTA N15-S15	σ CMa
	2000Feb08,10	2.16	0.32	IOTA N25-S15	σ CMa

Table 3. Calibrator Information (∗ indicates a calibrator of long-baseline IOTA interferometer data where accurate diameters are most critical).

Calibrator Name	Spectral Type	Adopted Uniform Disk[a] Diameter (mas)	Reference(s)
2 Cen	M4.5III	13.9 ±1.4	Heras et al. (2002)
14 Sgr	K2III	2.3±1.8	getCal[b]
54 Per	G8III	1.41±0.13	CHARM[c]
α Cet	M1.5III	11.6±0.4	CHARM
δ Vir	M3III	10.7 ± 1.0	Heras et al. (2002)
γ Hya*	G8III	3.4 ±0.5	getCal
HD 47667	K2III	2.56±0.04	CHARM
HD 63852*	K5III	2.3±1.7	getCal
o Tau*	G6III (SB)	2.7±0.3	CHARM, CADARS[d]
π Hya*	K2III	3.7±0.1	CHARM
π Leo*	M2III	4.85±0.23	CHARM
SAO 49410*	K5Iab	2.9±0.5	van Belle et al. (1999)[e]
SAO 104467*	K0V	1.7±0.3	getCal
SAO 104655	G8II-III	1.5±0.2	getCal
SAO 105500	M0III	5.5±0.5	CHARM
SAO 186681	K3III	6.9±0.9	getCal
SAO 186841*	K1III	4.4±0.2	CHARM
SW Vir	M7III	16.81±0.12	CHARM
σ CMa*	M0Iab	8.9±1.2	getCal
σ Vir*	M2III	6.2±1.0	getCal
ξ Cyg	K4.5I	6.0±1.3	getCal, CHARM

[a]The diameter error quotes have not been validated independently. While adequate for our purposes here, workers who require precision calibration are warned to research their calibrators carefully and not rely too heavily on "catalogs" such as CHARM.

[b]*getCal* is maintained and distributed by the Michelson Science Center (http://msc.caltech.edu)

[c]CHARM is the Catalog of High Angular Resolution Measurements (Richichi & Percheron 2002)

[d]CADARS is the Catalog of Apparent Diameters and Absolute Radii of Stars (Pasinetti-Fracassini et al. 2001)

[e]The diameter recorded in this reference is in error; however, the reported V^2 measurement is correct (van Belle, 2003, private communication) and we have

used this to calculate the UD diameter found herein.

Table 4. Results of Uniform Disk Fits

Source Name	Uniform Disk Diameter[a] (mas)	Comments
IK Tau	20.2±0.2±0.3	Large deviation from Uniform Disk See text for other provisos
NML Cyg	7.8±0.4±0.5	Unexpectedly small; large gap in baseline coverage
R Hya	23.7±0.8±0.6	Some deviation from Uniform Disk ($\chi^2 \sim 2$)
R Leo	30.3±0.2±0.3	Excellent fit to Uniform Disk
RT Vir	12.4±0.1±0.4	Good fit
VX Sgr	8.7±0.3±0.1	Excellent fit (IOTA data only)
VY CMa	18.7±0.3±0.4	Good fit; star contributes 36% of Kband flux
W Hya	42.5±0.7±0.4	Poor fit ($\chi^2 \sim 5$)

[a]The best-fit UD diameter (for $\lambda_{\rm eff} = 2.16\mu$m) is followed by estimates of the statistical error, then by an estimate of the systematic error (see text in §3.4). The systematic error is usually dominated by uncertainty in the calibrator diameter. We emphasize that we measure an apparent diameter, and relation to the true "photospheric" diameter relies on additional assumptions of limb-darkening and other effects; some late-type stars are known to have different apparent sizes between the visible, near-IR and mid-IR wavelengths (e.g., Weiner et al. 2000).

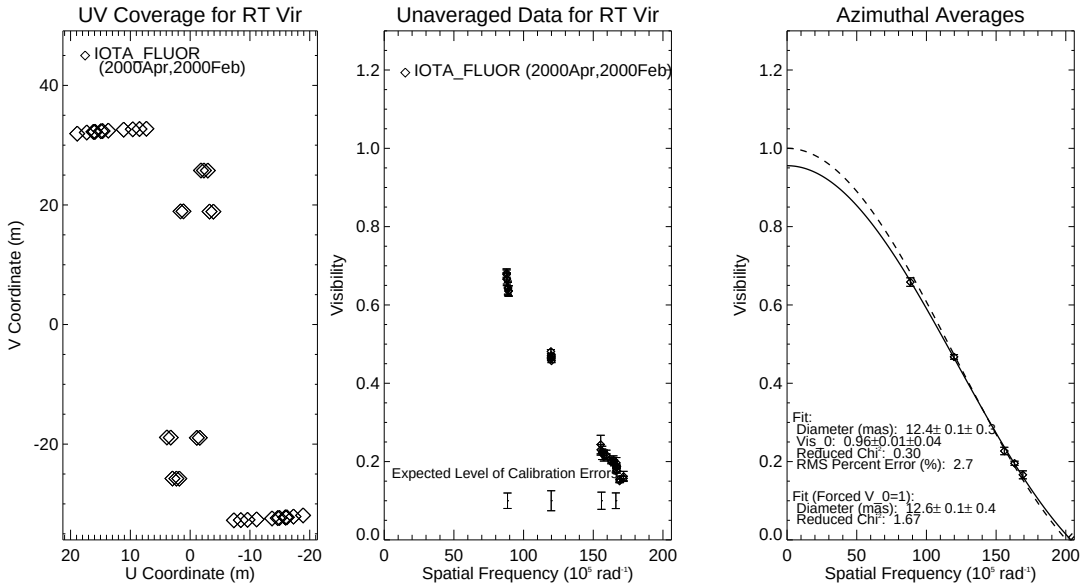

Fig. 1.— a) UV coverage of the RT Vir observations with IOTA-FLUOR. b) Unaveraged data for RT Vir. Error bars at the bottom of this panel show the expected level of calibration errors, due to uncertainties in calibrator diameters (which generally dominate at long baselines) and unmodelled chromatic effects (which become important for high visibilities); see §3.4.1 for the detailed estimation procedure. c) Averaged data with uniform disk fits. Here, we present fits with both V(0) fixed to 1.0 and also left free to vary. See text §3.4 for discussion.

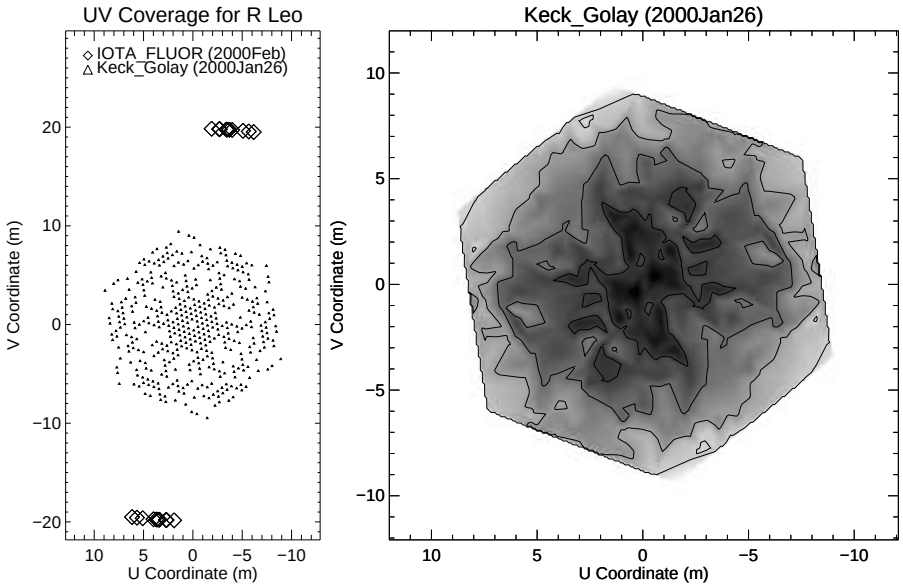

Fig. 2.— a) UV coverage of the R Leo Observations from Keck aperture masking and IOTA-FLUOR. b) Two-dimensional visibility data observed using Keck aperture masking. Each contour is 0.1 Visibility.

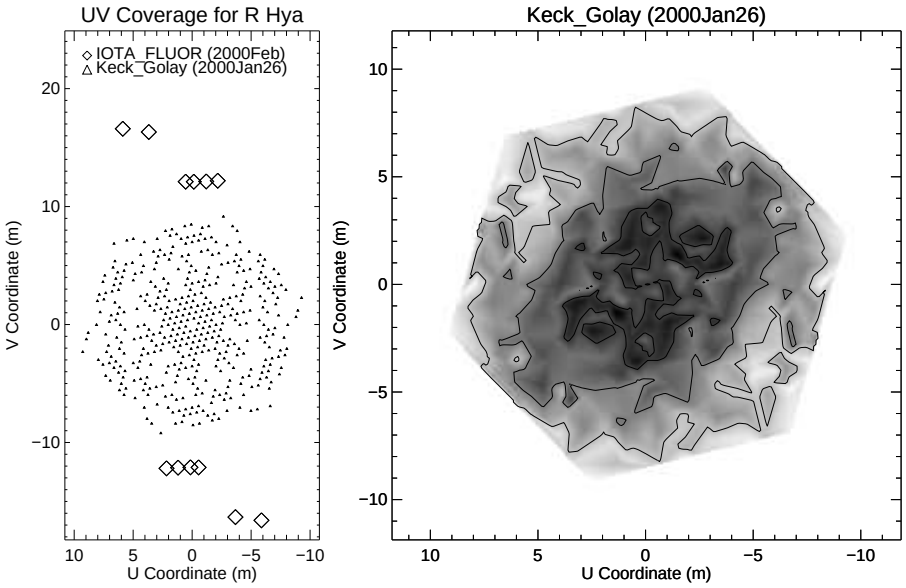

Fig. 3.— Same as Figure 2, except for R Hya.

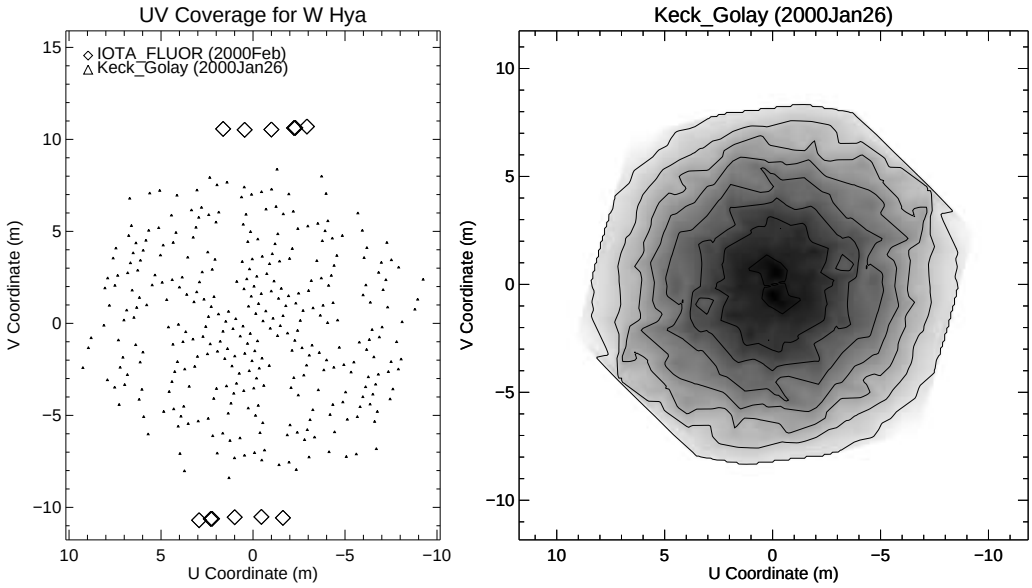

Fig. 4.— Same as Figure 2, except for W Hya.

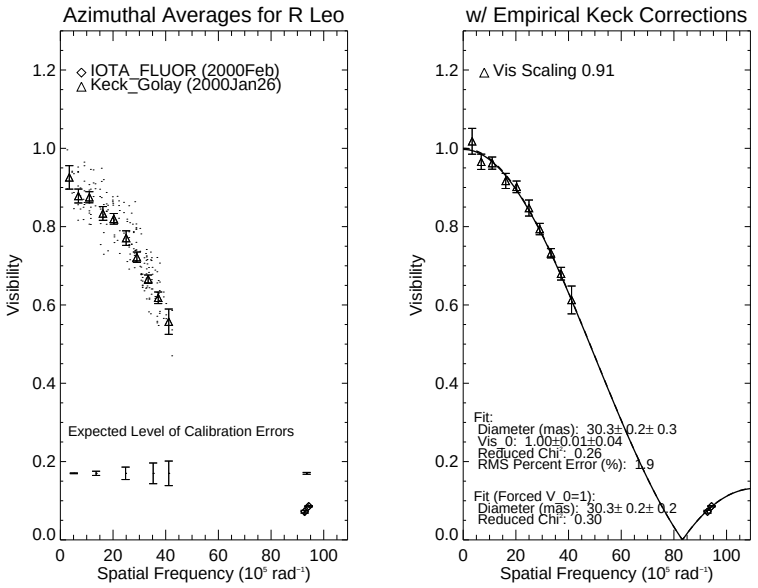

Fig. 5.— R Leo Data. a) The left panel shows each individual Keck and IOTA visibility datum as a point, while the azimuthal averages are plotted with error bars. At the bottom, an estimate of the calibration/systematic errors are shown for each baseline range. b) The right panel shows only averaged data and the empirical Keck corrections have been applied (see §3.3). Two curves are shown: solid line is a uniform-disk diameter fit where V_0 is a free parameter, dashed line is a fit with fixed V_0=1.0. The fitted parameters and reduced χ^2 are included in the legend. Two errors are listed for each fitted parameter, corresponding to the statistical and systematic uncertainties respectively. (The solid and dashed lines are indistinguishable for these particular data fits.)

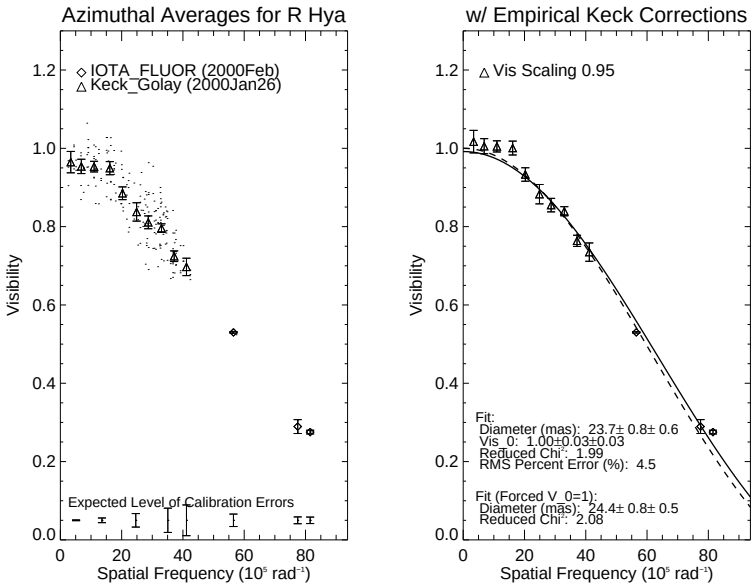

Fig. 6.— Same as Figure 5, except for R Hya.

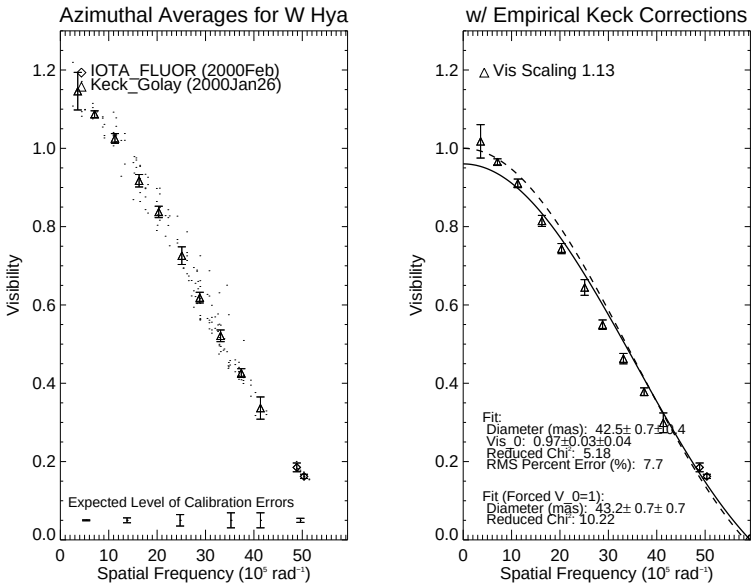

Fig. 7.— Same as Figure 5, except for W Hya.

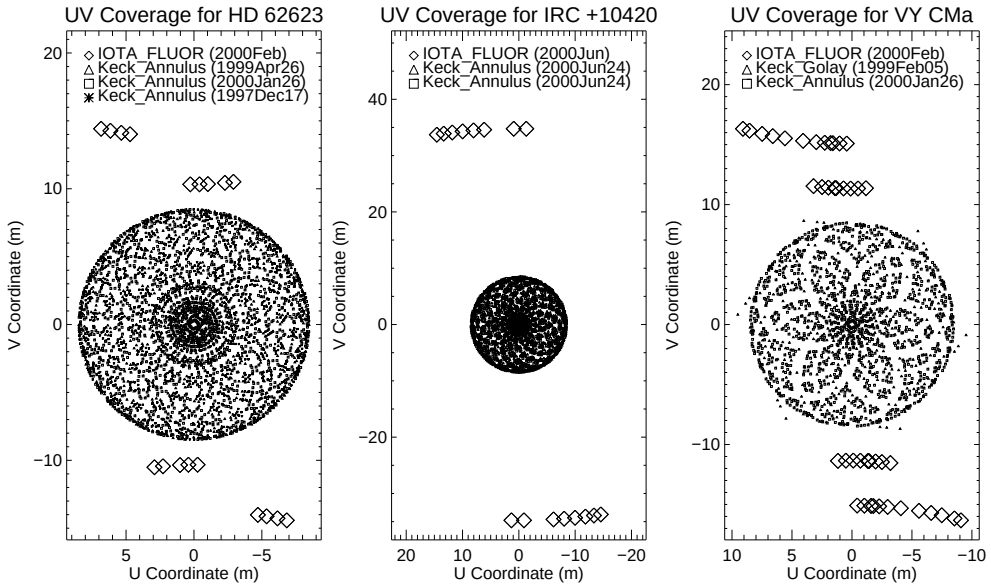

Fig. 8.— UV coverage of the new interferometric observations for: a) HD 62623, b) IRC +10420, c) VY CMa

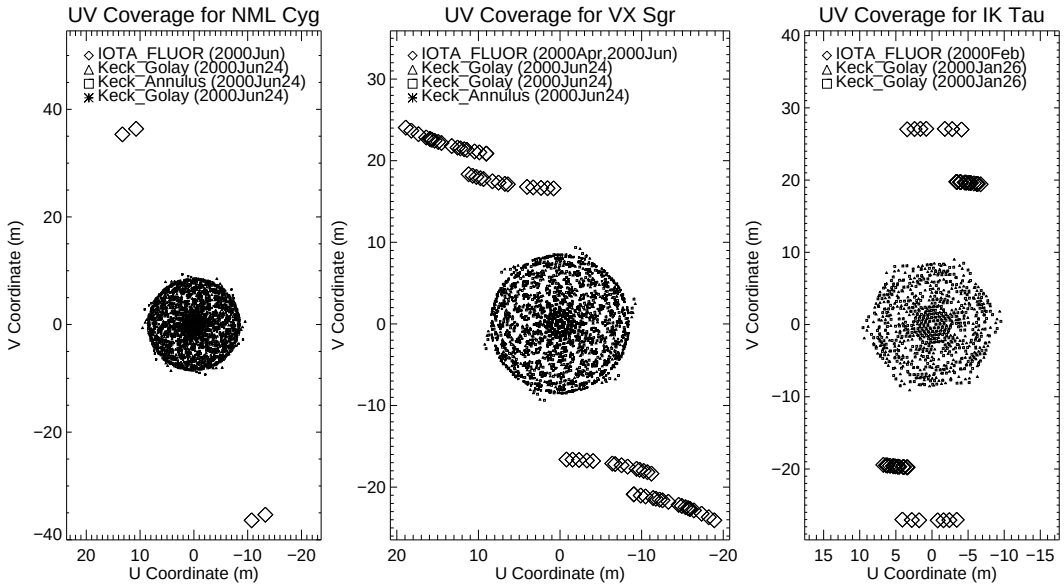

Fig. 9.— UV coverage of the new interferometric observations for: a) NML Cyg, b) VX Sgr, c) IK Tau

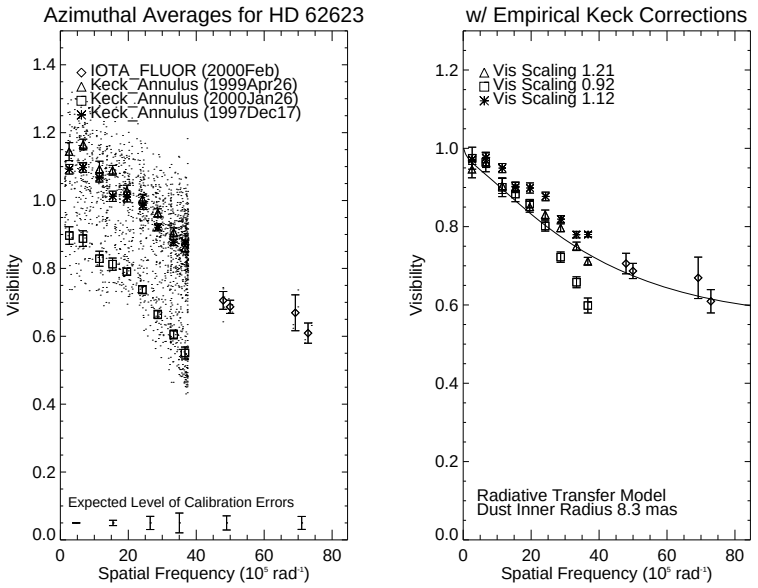

Fig. 10.— HD 62623 Data. a) The left panel shows each individual Keck and IOTA visibility datum as a point, while the azimuthal averages are plotted with error bars. At the bottom, an estimate of the calibration/systematic errors are shown for each baseline range. b) The right panel shows only averaged data and the empirical Keck corrections, particularly large for this source, have been applied (see §3.3). The solid line represents the radiative transfer model fit discussed in the text (§4.1).

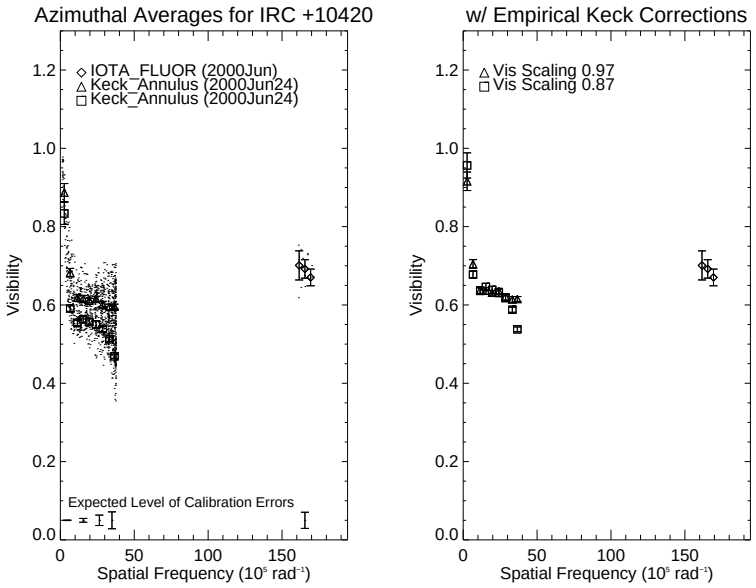

Fig. 11.— Same as Figure 10, except for IRC +10420 data.

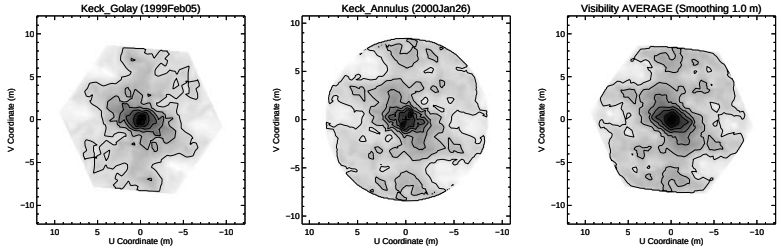

Fig. 12.— Visibility data for Keck aperture masking observations of VY CMa: 1999 February (left panel), 2000 January (middle panel), averaged and smoothed (right panel). Each solid contour line represents 0.10 in visibility

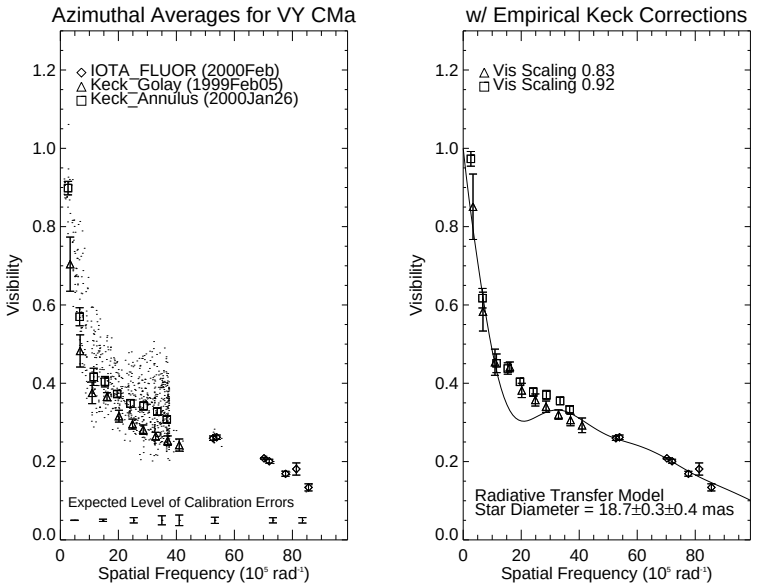

Fig. 13.— Same as Figure 10, except for VY CMa data. The solid line shows the visibility prediction from a simple radiative transfer model (see §4.3).

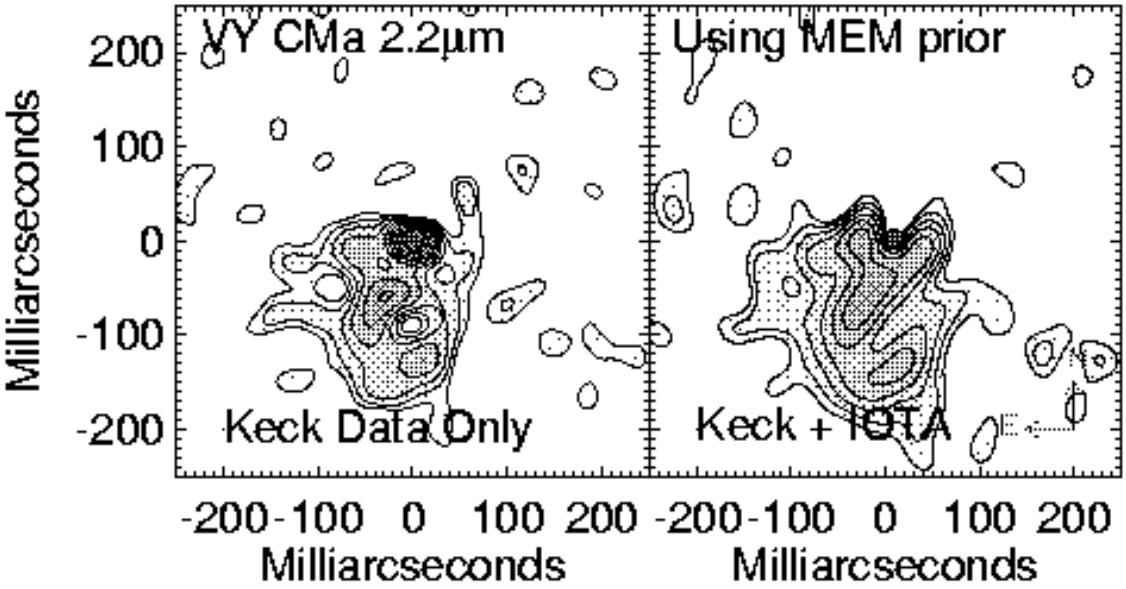

Fig. 14.— Maximum entropy image reconstructions of the VY CMa circumstellar environment. The left panel shows an image reconstruction using Keck masking data only and a uniform prior. The right panel shows an image reconstruction using a MEM prior incorporating a 18 mas disk in the center of the asymmetric nebula (see text for further details); the star is shown here actual size. The lowest contour level in each figure represents a 2-σ noise level above the background; the subsequent contours are logrithmically-spaced, increasing by a factor of 2 for each level. For reference, the 1-σ noise limits are 0.09% and 0.026% of the peak for the left and right panel respectively, a scaling due to the difference in the compactness of the central source.

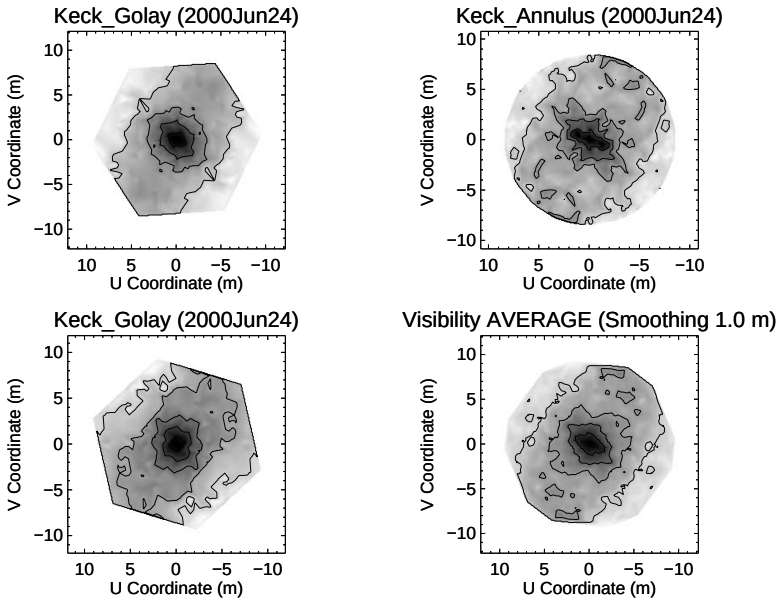

Fig. 15.— Visibility data for Keck aperture masking observations of NML Cyg (three measurements from 2000Jun); the bottom-right panel is the average of the other three, and has been slightly smoothed. Each solid contour line represents 0.10 in visibility. The NE-SW elongation of the source (in visibility space, the source is more resolved along the NE-SW axis) is real and reflects a bipolar dust distribution imaged in Figure 17.

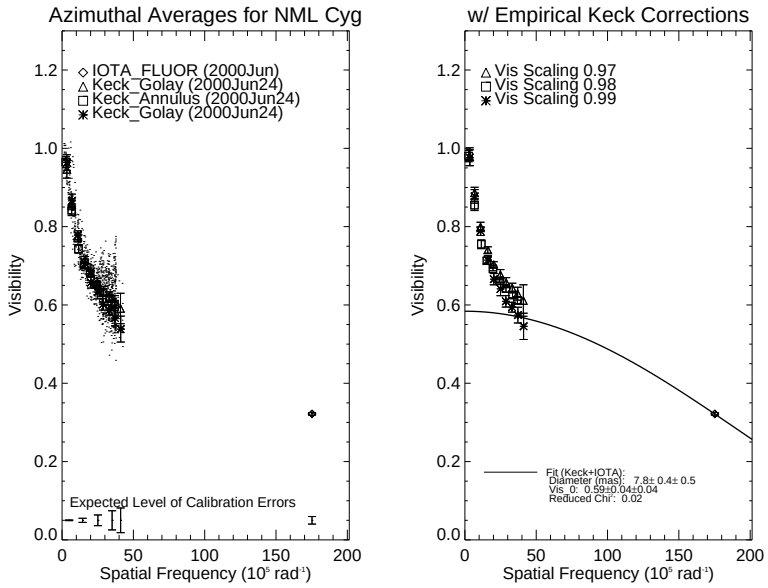

Fig. 16.— Same as Figure 10, except for NML Cyg data. The solid line shows a uniform disk fit to the longest baseline visibility data.

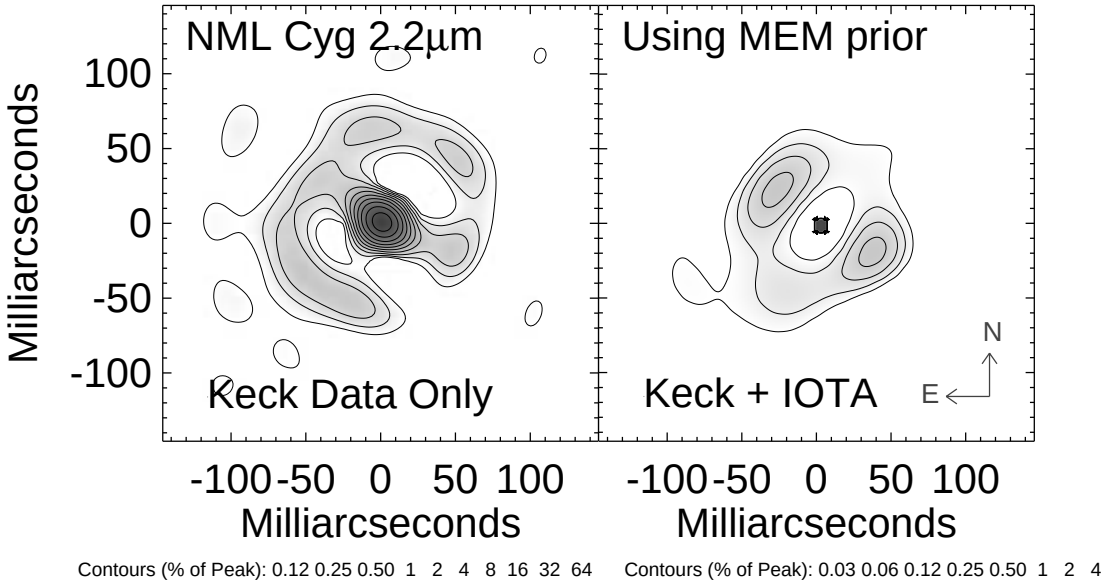

Fig. 17.— Maximum entropy image reconstructions of the NML Cyg circumstellar environment. The left panel shows image reconstruction Keck masking data only, using a uniform prior. The right panel shows an image reconstruction using a MEM prior with 59% of the flux in a single 7 mas pixel (the star is shown here actual size). This image reconstruction allows a high fidelity dust shell image to be created by constraining the size and amount of compact stellar emission (based on IOTA data). The logarithmic contour levels each represent a factor of 2 in surface brightness compared to the peak. for the left panel, we have 0.125, 0.25, 0.5, 1, 2, 4, 8, 16, 32, and 64% respectively; for the right panel, we have 0.03125, 0.0625, 0.125, 0.25, 0.5, 1, 2, and 4% respectively.

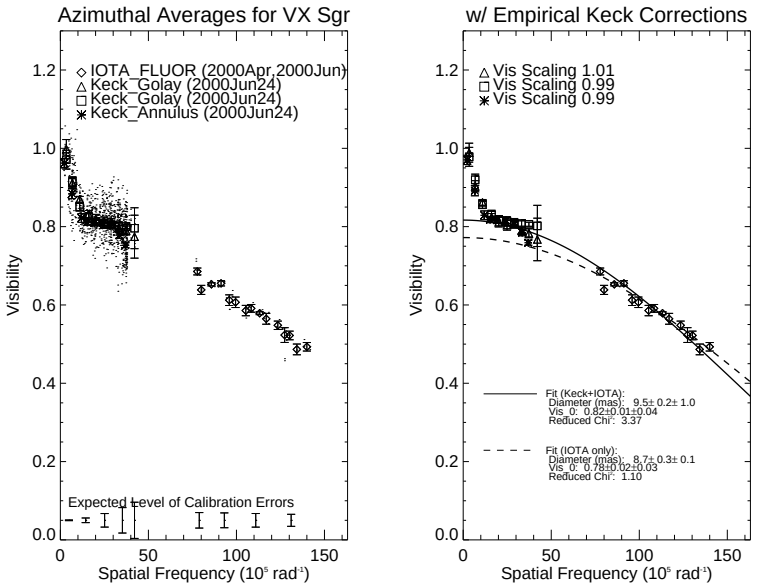

Fig. 18.— Same as Figure 10, except for VX Sgr data. The solid and dashed lines show two different Uniform Disk fits to the stellar photosphere (see §4.5 for further information).

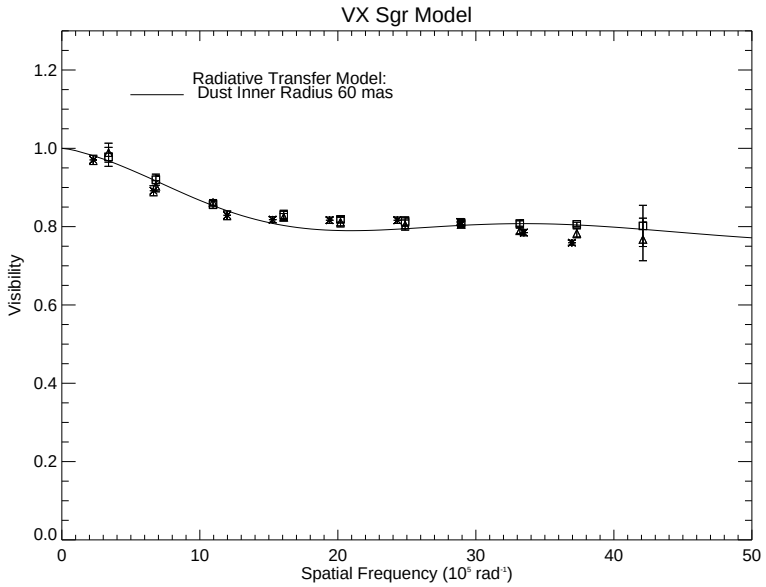

Fig. 19.— This figure shows the radiative transfer fit to the VX Sgr 2.2μm visibility data.

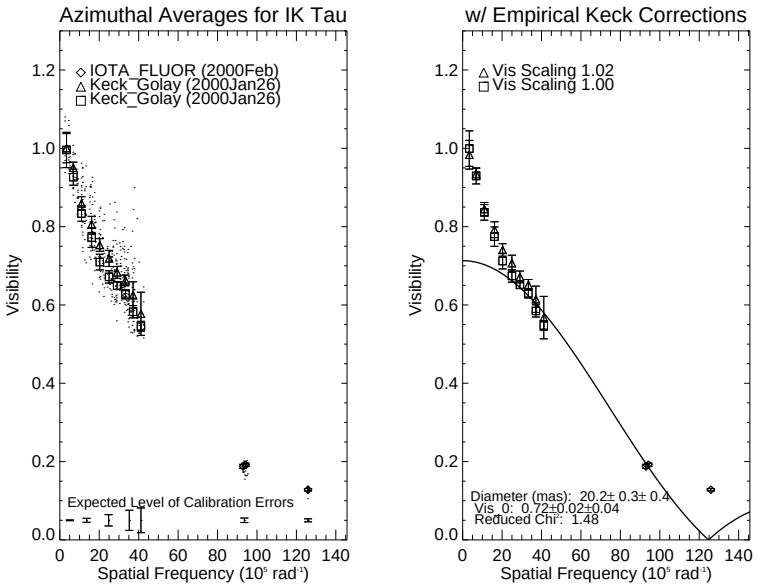

Fig. 20.— Same as Figure 10, except for IK Tau data. The solid line shows a uniform disk fit which ignores the visibility datum at ∼27 m baseline (see text §4.6 for justification).

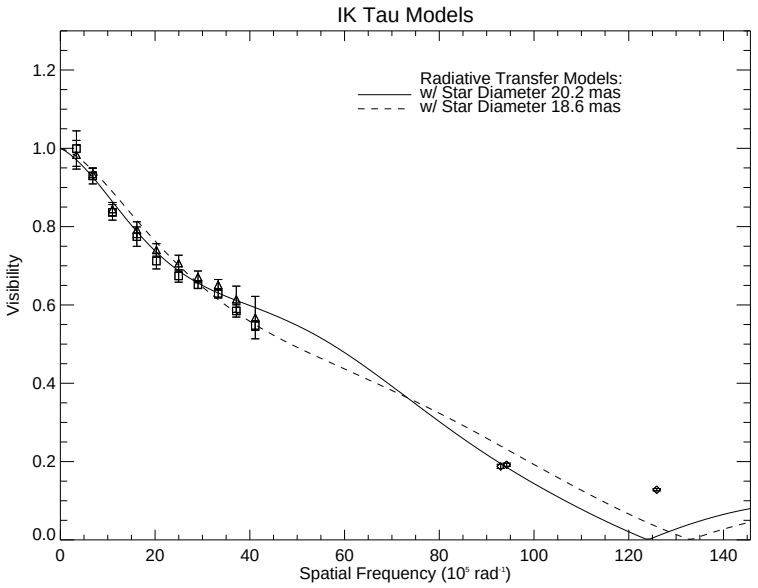

Fig. 21.— This figure shows results of two fits to the IK Tau 2.2μm visibility data using simple radiative transfer models. The fit to the short baseline data is noticeably better using a stellar diameter of 20.2 mas than 18.6 mas; diameters smaller than this range require dust temperature $\gtrsim$1500 K. The disagreement between models and the data at the longest baselines may be due to deviations from uniform brightness across the photosphere of this highly evolved giant star (M10III).

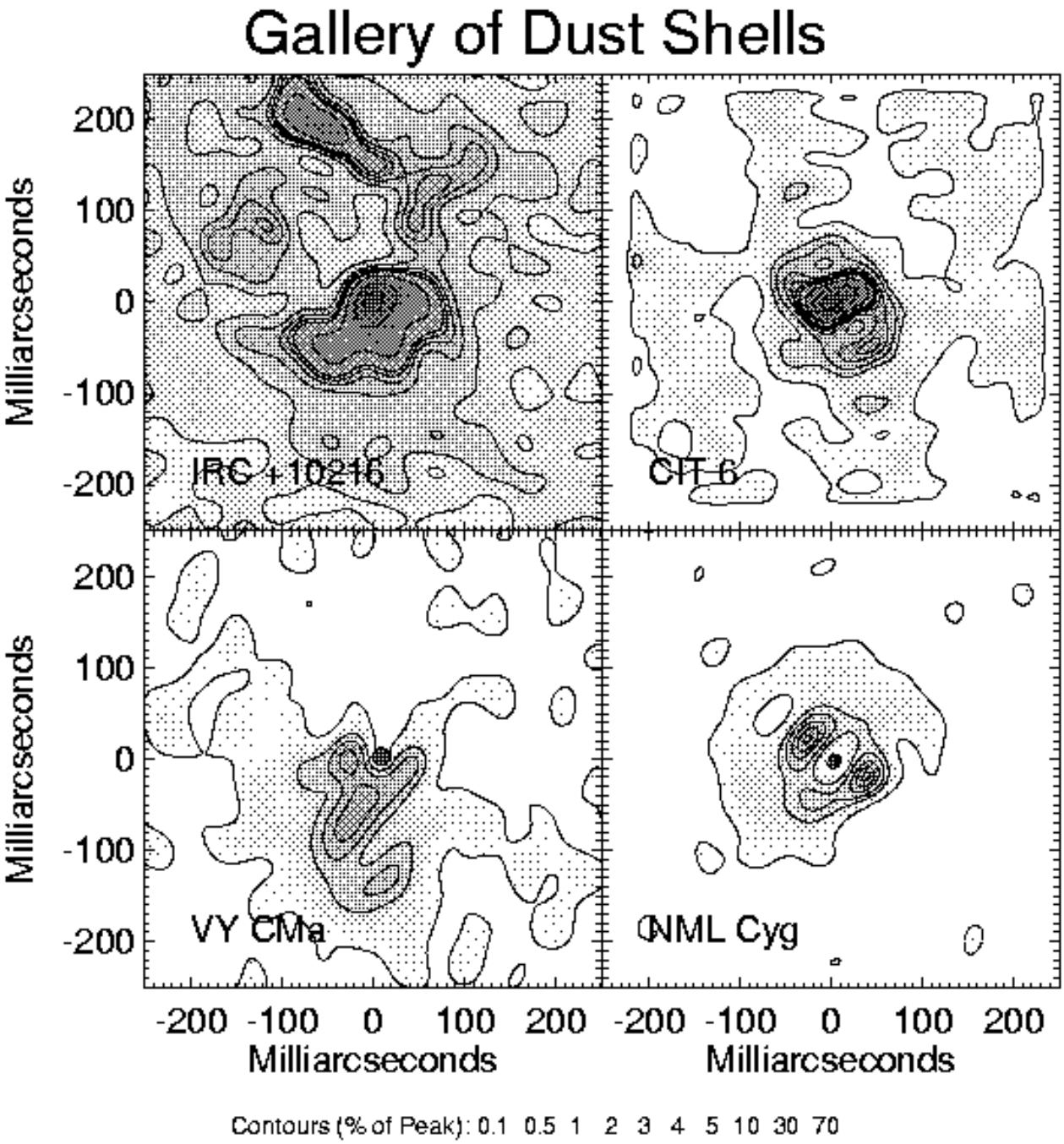

Fig. 22.— This figure shows 2.2μm images of mass-losing evolved stars reconstructed using Keck aperture masking data. The images of the carbon stars IRC +10216 and CIT 6 are from Tuthill et al. (2000a) and Monnier et al. (2000b) respectively, while the images of VY CMa and NML Cyg are from this work and have incorporated long-baseline IOTA data. The contours levels are 0.1, 0.5, 1, 2, 3, 4, 5, 10, 30, and 70% of the peak brightness in each panel, except for NML Cyg where the contours levels are 10×smaller (owing to its fainter dust shell and more compact central source). Although circularly-symmetric dust shells likely exist, we have yet to image one successfully using optical interferometric techniques.

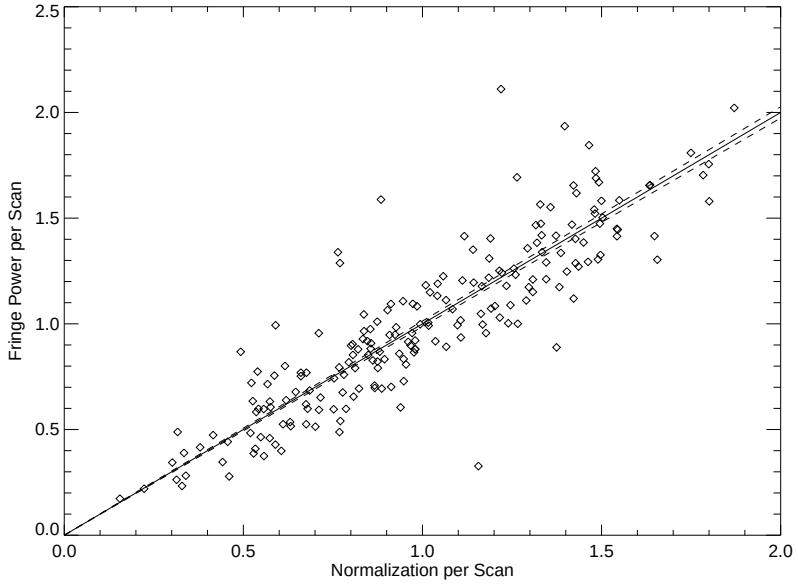

Fig. 23.— Normalization Scheme. This figure illustrates the new calibration method being employed for analyzing IOTA-FLUOR data. The (bias-corrected) fringe power observed in each fringe scan (of 200) is plotted against a "normalization" factor estimated from the photometric channels of FLUOR. The V^2 is simply proportional to the slope of this relation, which is plotted here along with its uncertainty. For this single dataset, the formal uncertainty in the slope is 1.3% in V^2, which is only 0.65% for the Visibility.